REVIEW

Chemical Synthesis, Characterization and Properties of Multi-Element Nanoparticles

Kohei Kusada,[a, b] Megumi Mukoyoshi,[a] Dongshuang Wu,[a] Hiroshi Kitagawa*[a]

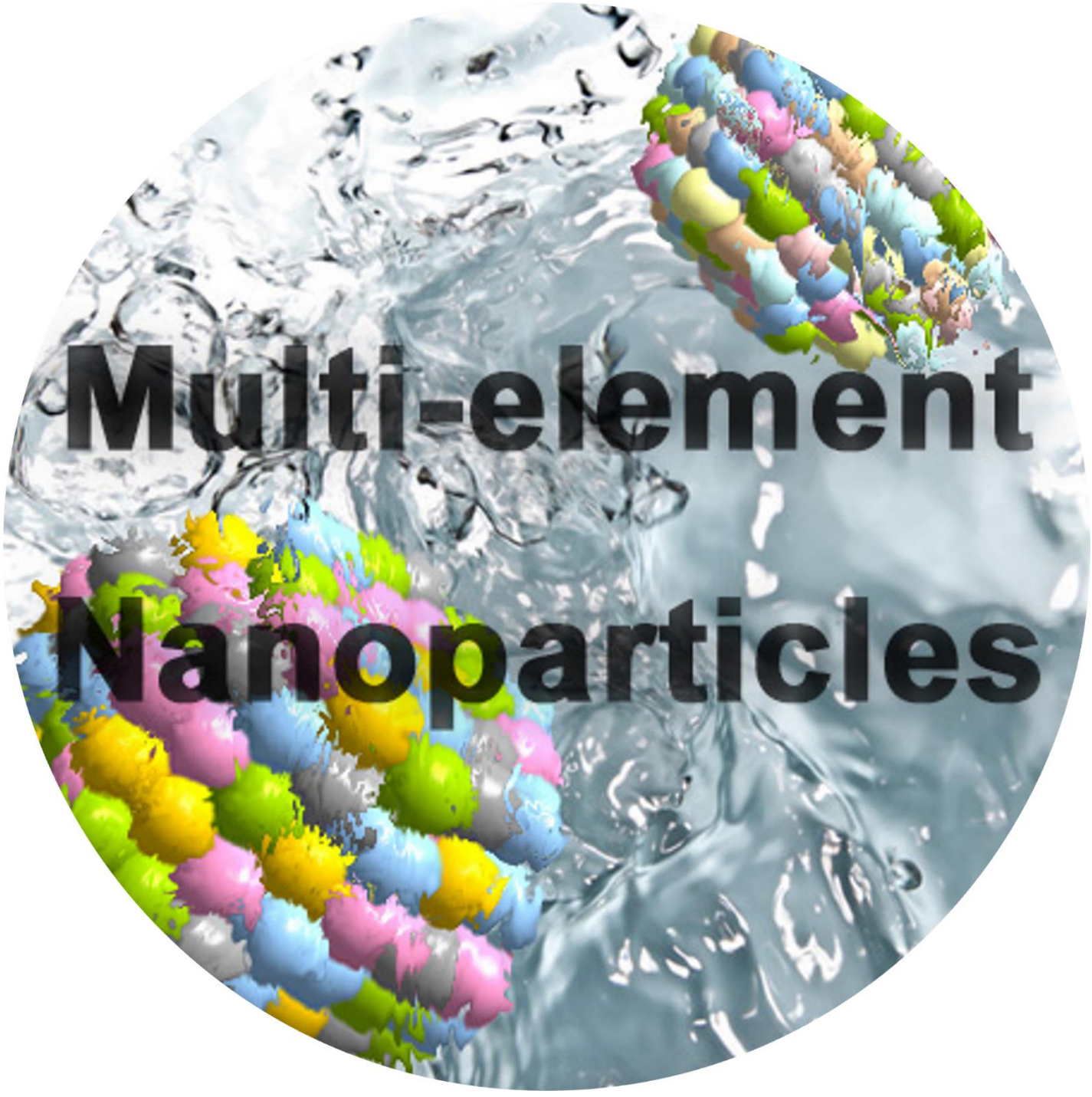

[a] Dr. K. Kusada, Dr. M.Mukoyoshi, Dr. D. Wu, Prof. H. Kitagawa
Division of Chemistry, Graduate School of Science,
Kyoto University
Kitashirakawa-Oiwakecho, Sakyo-ku, Kyoto, 606-8502, Japan
E-mail: Kitagawa@kuchem.kyoto-u.ac.jp
[b] Dr. K. Kusada
The Hakubi Center for Advanced Research
Kyoto University
Kitashirakawa-Oiwakecho, Sakyo-ku, Kyoto, 606-8502, Japan

Abstract: Multi-element nanoparticles (NPs) consisting of five or more elements have been increasingly studied in the past 5 years. Their emergence is taking materials science one step further because they exhibit superior properties to conventional NPs in a range of respects, including catalysis. This review focuses on the recent progress in multi-element NPs regarding synthesis, especially in regard to chemical synthesis, characterization, and properties. We begin with a brief introduction of the multi-element NPs and an overview of their synthesis methods. Then, we present representative examples of multi-element alloy NPs and ceramic NPs, including oxide NPs prepared by chemical syntheses. This review intends to provide useful insights into the chemical methods that are used to synthesize multi-element NPs, and includes a discussion on the possibilities arising from their use in new functional materials.

KK received his PhD in 2013 at Kyoto University under the supervision of Prof. Hiroshi Kitagawa. He worked as a researcher at Asahi Kasei Chemicals Co. before moving back to Kyoto University to work as an Assistant Professor, later becoming an Associate Professor of the Hakubi Center at Kyoto University. He has also been a researcher for JST-PRESTO. His current interests focus on the design of advanced functional nanoparticles for catalysis.

MM graduated from Kyoto University in 2014 (MSc, Chemistry), after which she worked as a researcher at Showa Denko K. K. (2014–2017) and Daikin Industries, Ltd. (2018–2021). She returned to Kyoto University and obtained her PhD in 2022, and then became an Assistant Professor. Her current research focuses on the design of nanomaterials based on metal nanoparticles and metal–organic frameworks.

DW received her PhD in 2014 at the University of Chinese Academy of Sciences. Since then, she worked as a postdoc and became an Assistant Professor at Kyoto University. Her current research focuses on the design of metal-based nanomaterials.

HK finished his PhD at Kyoto University in 1991 and, after working as an Assistant Professor at the Institute for Molecular Science (IMS) and the Japan Advanced Institute of Science and Technology (JAIST), in 2000, he was appointed Associate Professor at University of Tsukuba. He became a Professor of Chemistry at Kyushu University in 2003 and a Professor at Kyoto University in 2009. He then worked as the Vice Provost and Deputy Executive-Vice President for Research at Kyoto University. He was also engaged at JST as a Research Director of ACCEL, and is currently the Director of the network-type research institution Exploring Innovative Materials in Unknown Search Space, CREST. He has published more than 470 original research papers dealing with solid-state chemistry, coordination chemistry, nanoscience, low-dimensional electron systems, and molecular-based conductors.

1. Introduction

There are about 120 elements on the periodic table, and all natural and artificial materials are composed of their combinations. The properties of these materials have been generally improved by mixing some elements into the main elements, for example, Fe-based alloys and Ce-based oxides.[1,2] To overcome the limitations of this conventional approach, increasing numbers of studies have recently focused on multi-element alloys. In particular, the idea of high-entropy alloys (HEAs) consisting of five or more elements with equal or relatively large compositions was proposed in the early 2000s,[3,4] and this approach has become very popular. For such alloys, we cannot define the main component, and they often show unexpected properties that are not observed in the constituents themselves (known as the “cocktail effect”). This could be a game-changer that would transform how functional materials are designed and release us from the preconceived image of the elements. Although studies on multi-element materials started from the mechanical properties of solid-solution alloys, they have recently expanded to include the synthesis of not only alloys, but also ceramics, and to investigate their thermoelectric, magnetic, and ion-conducting properties.[5]

Nanoparticles (NPs) have attracted attention because their physical and chemical properties differ from those of their bulk forms because of their large surface-to-volume ratio and the quantum size effect.[6] To enhance their unique properties, many types of synthesis techniques have been developed for not only metal NPs, but also ceramic NPs. Chemical synthesis is one of the best ways to tune the particle size,[7–9] morphology,[10–13] and composition[14–16] of NPs and obtain new materials that cannot be found in bulk states[17–21] because NPs are built up from metal ions at the atomic level during reaction in a solution. As with bulk materials, mixing some elements into the main elements is also known to improve properties, and many binary and ternary alloy NPs and ceramic NPs have been investigated.[22–25] After the explosive growth in the number of studies on multi-element alloys, research since 2018 on multi-element alloy NPs, including HEA NPs, has been extensive.[26–33] Mirroring the development of alloy NPs, multi-element ceramic NPs, including oxide, sulfide, and carbide NPs, have been reported,[34–41] describing attractive properties such as high catalytic activity and stability. In addition, the number of studies on multi-element NPs is increasing year-by-year.

For multi-element NPs, configurational entropy S is much larger than in binary systems because, with a simple calculation, the number of atomic configurations in a crystal structure increases exponentially with an increasing number of constituents.[3] However, this is not perfectly correct. It is reported that chemical short-range order in a multi-element solid-solution phase affects the number of atomic configurations. The chemical short-range order is developed by the heat of mixing of immiscible elements and local lattice distortion. Therefore, in a precise sense, the number of atomic configurations depends on not only the number of constituents but also the overall thermal history of the solid.[42] Therefore, considering Gibbs free energy, $G = H - TS$, synthesis at higher temperatures is considered to be favorable for obtaining a single solid-solution phase in which all constituents are randomly and homogeneously distributed. However, since high temperature also accelerates particle growth and sintering, it is difficult to apply simply the synthesis techniques of bulk HEAs

and high-entropy ceramics (HECs) to synthesize multi-element NPs. In addition to the synthetic challenges, for multi-element NPs, characterization and understanding of the mechanism of their properties become much more difficult because many kinds of elements exist in a nanometer-sized particle.

In this review, we focus on recent progress in the development of multi-element NPs, including alloys and ceramics, in regard to synthesis, especially in chemical synthesis, characterization, and properties. Although the history of synthesis for multi-element NPs is relatively new, we would like to introduce mainly wet-chemical synthesis because the wet-chemical method is well developed in monometallic NPs and allows the size, morphology, and composition of multi-element NPs to be finely tuned. We begin with a brief introduction of multi-element NPs and present an overview of their synthesis methods. Then, we discuss representative examples of multi-element alloy NPs and ceramic NPs, including oxide NPs prepared by chemical syntheses. This review intends to provide useful insights into the chemical methods that are used to synthesize multi-element NPs, and to discuss the possible use of such NPs as new functional materials.

2. Overview of Multi-element NPs

2.1. Overview of Multi-element NP Synthesis Methods

Figure 1 shows the number of publications related to multi-element NP synthesis. To investigate trends in synthesis methods for multi-element ceramic NPs as well as alloys, we used “high-entropy” and “nanoparticle” as search keywords. Since the carbothermal shock (CTS) method was reported by Yao et al. in 2018,[26] reports on multi-element NPs, especially those that have five or more elements, have increased drastically. These synthetic methods can be classified into four categories: pyrolysis, chemical synthesis, mechanochemical synthesis, and the top-down method.

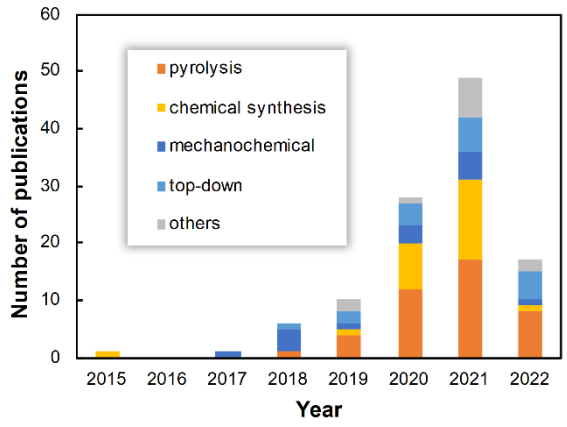

Figure 1. The number of publications related to multi-element nanoparticle synthesis using the keywords “high-entropy” and “nanoparticle” to search SciFinder (March 2022). Orange: pyrolysis, yellow: chemical synthesis, blue: mechanochemical synthesis, light blue: top-down method, and gray: others.

2.1.1. Pyrolysis

Pyrolysis is the most common method to obtain multi-element NPs. In the typical case, metal salt precursors mixed in a solution are loaded on supports such as carbon materials and alumina. A subsequent heating process decomposes the salts to produce NPs. In particular, rapid heating and cooling processes such as the CTS method and fast-moving bed pyrolysis[43] have been studied intensively because these methods enable the formation of solid-solution NPs, even in immiscible elemental combinations. Alternatively, sol-gel materials or metal–organic complexes such as metal–organic frameworks (MOFs) can be used as a precursor.[40,44] In addition to HEAs, high-entropy oxides, sulfides, phosphides, and carbides are also increasingly synthesized by using pyrolysis methods.

2.1.2. Chemical Synthesis

Multi-element NPs can be synthesized from multiple metal salts in solution by chemical reaction, such as reduction, hydroxylation, and sulfurization. The details are discussed in the following sections.

2.1.3. Mechanochemical Synthesis

Mechanochemical synthesis is a classical method used for bulk HEAs and NPs. Multiple metal powders and supports are mixed with stainless steel or ceramic balls, and multi-element NPs are obtained by homogeneously milling the mixture.[39,45] The greatest advantage of this approach is its simplicity and ease of scale-up. Several patents have been filed in this field.

2.1.4. Top-down Method

In the top-down method, multi-element NPs are synthesized from bulk metal sources using breakdown methods such as laser ablation, sputtering, and arc-discharge techniques.[29,46] These methods provide NPs without any protective agents. As metal sources for the top-down method, both single element targets and pre-alloyed ingots can be used.[32,47]

2.1.5. Other Methods

Various other methods for synthesizing multi-element NPs have been developed; however, there are few reported cases, electrodeposition being one of them. By extending the CTS method, in this technique, metal precursors confined in water nanodroplets are rapidly reduced by electro-shock.[48]

2.2. Chemical Synthesis Method of Multi-element NPs

Chemical synthesis methods have been used to synthesize monometallic and bimetallic NPs,[49–51] and the approach has recently been extended for the synthesis of multi-element NPs. In the chemical synthesis method, multi-element NPs are synthesized in a bottom-up manner from multiple metal salts in solution, and well-dispersed NPs are easily obtained. One of the advantages of the chemical synthesis method is that NPs with small sizes such as in the 1–5 nm range can be obtained because the synthesis can be carried out under milder temperature conditions (<300°C) than that required for other methods such as pyrolysis techniques. These features make this method promising for developing efficient catalysts, which require many reaction

sites on the surface. The reported chemical syntheses of multi-element NPs, especially focusing on five or more elements, are summarized in Table 1. The number of reports on multi-element NPs using chemical synthesis has been increasing since 2015. Most of these refer to metal NPs, which are synthesized by using reducing agents such as $NaBH_4$ and $LiBEt_3H$. Solvents such as ethanol, ethylene glycol (EG), and triethylene glycol (TEG), and protective agents such as oleylamine, can also serve as reducing agents. Multi-element oxide NPs are also synthesized by a chemical reaction in the presence of alkali. In many cases, the chemical reactions are carried out under mild heating, and microwave heating is also used. The details are discussed in the following sections.

Table 1. Summary of high-entropy nanoparticles synthesized by chemical synthesis and their synthesis conditions.

Element	Temp. [°C]	Reductant / additional agent	Solvent	Protective agent	Size [nm]	Structure	Properties	Ref.
NiFeCrCuCo	250	$LiBEt_3H$	benzyl ether	oleic acid/ oleylamine	26.7	fcc	–	[52]
PtAuPdRhRu	RT	EG[a]	EG	–	2.8	fcc	catalysis	[53]
CoCuMgNiZnO	400	–	H_2O/EtOH/EG	Pluronic P123	5	spinel	catalysis	[38]
PtIrPdRhRu	200	EtOH	EtOH/acetone	–	200	fcc	–	[31]
RuRhPdOsIrPt	230	TEG[b]	TEG	PVP[c]	3.1	fcc	catalysis	[54]
CrMnFeCoNiO	140	urea	water	CATB[d]	100–200	spinel	capacitance	[55]
$BaSr(ZrHfTi)O_3$, $BaSrBi(ZrHfTiFe)O_3$, $Ru/BaSrBi(ZrHfTiFe)O_3$	RT	NaOH	water	–	5.9	perovskite	catalysis	[56]
PtNiFeCoCu	220	oleylamine/glucose/$Mo(CO)_6$	oleylamine	CTAC[e]/ oleylamine	3.4	fcc	catalysis	[30]
IrPdPtRhRu	230	TEG	TEG	PVP	5.5	fcc	catalysis	[57]
PdCuPtNiCo	236	oleylamine	oleylamine/ octadecene	oleylamine	10.4	B2(PdCu)core/ PtNiCo shell	catalysis	[58]
ZnCoCuInGaS	140	di-tert-butyl disulfide	oleylamine/ octadecene/ benzyl ether	trioctylphosphine	13	wurtzite-type	–	[59]
PtPdFeCoNi	microwave	–	–	–	12.8	fcc	–	[60]
(MgCuNiCoZn)O	microwave	NH_4OH	water	–	60–100	amorphous	Li-ion storage	[61]
NiCoFePtRh, PtRhAuIrPd, CoCuAnPtPd, NiCoCuPtAu, CdNiPtIrPd, CoNiCdPtPdIr, CoCdPtPdIrAu, CoNiCuCdPtPdIr, FeCoNiCuCdPtIrPd	RT	$NaBH_4$	H_2SO_4/water	–	1.68	fcc	catalysis	[62]
FeCoNiCuSn	RT	$NaBH_4$	HCl/EG	–	8–135	intermetallic	capacitance	[63]
RuFeCoNiCu	220	oleylamine	oleylamine	oleylamine	15–16	hcp	catalysis	[64]
PdFeCoNiCu	220	oleylamine	oleylamine	oleylamine	34	bcc	catalysis	[65]

AuHgPdPt	RT	–	water	sodium citrate	30–40	fcc	catalysis	[66]
AuPdPtRhRu	RT	ionic liquid	water/ionic liquid	–	3	fcc	catalysis	[67]
RuRhPdAgOsIrPtAu	230	TEG	TEG	PVP	4	fcc	catalysis	[24]
PtRuNiCoFeMo	210	oleylamine/glucose	oleylamine	STAB[f]/ oleylamine		fcc	catalysis	[28]
IrPdPtRhRu	230	TEG	TEG	carbon	4.6	fcc	catalysis	[68]
IrPdPtRhRu	300	Ethanol	NaOH/H_2O	PVP	3.1	fcc	–	[69]
IrPdPtRhRu	RT	??	THF	carbon	1.32	fcc	catalysis	[70]

[a] EG: ethylene glycol. [b] TEG: triethylene glycol. [c] PVP: polyvinylpyrrolidone. [d] CATB: (1-Hexadecyl)trimethylammonium bromide. [e] CTAC: (1-Hexadecyl) trimethylammonium chloride. [f] STAB: trimethyl ammonium bromide.

3. Chemical Synthesis and Properties of Multi-element Alloy NPs

3.1. Synthetic Methods of Multi-element Alloy NPs

For clarity, we confined the chemical synthetic method to (1) solution-based reactions and (2) reduction by a reducing agent. The first report can be traced to 2015, when Singh and Srivastava reported the formation of NiFeCrCuCo NPs by injecting a strong reducing agent, namely superhydride ($LiBEt_3H$), into a reaction mixture of benzyl ether, oleic acid, oleylamine, and metal precursors under a 250°C and Ar atmosphere.[52] The authors claimed that "there exists a particle-to-particle compositional distribution between the nanoparticles in the as-synthesized nanoparticle dispersion". After 4 years, Liu and coauthors reported an ultrasonication-assisted wet chemistry method to synthesize carbon-loaded PtAuPdRhRu alloy NPs with around a 3 nm diameter.[53] In localized microscopic regions, formation, successive growth, and implosive collapse of microscopic bubbles occurs, which can achieve extremely high temperatures (ca. 5000°C) for momentary time spans (< 10^{-9} s).[71,72] The as-prepared NPs were dual fcc phases that changed into a single fcc phase after high-temperature annealing at 700°C in an N_2 atmosphere. We note that one of the definitions of HEA is single-phase. In 2020, Broge et al.[31] explored the possibility of obtaining PtIrPdRhRu HEAs by a one-pot solvothermal process. The homogeneous distribution of each element for NPs with larger sizes was evident. Whereas the stoichiometries varied for smaller particles; for example, some NPs have a Pd-rich tail. The authors concluded that "HEA solvothermal synthesis is possible, but the product is slightly inhomogeneous with a minor fraction of particles deviating from the main HEA phase". After the three early reports noted above, various chemical synthetic methods have been reported to afford well-defined multiple-elemental alloy NPs.

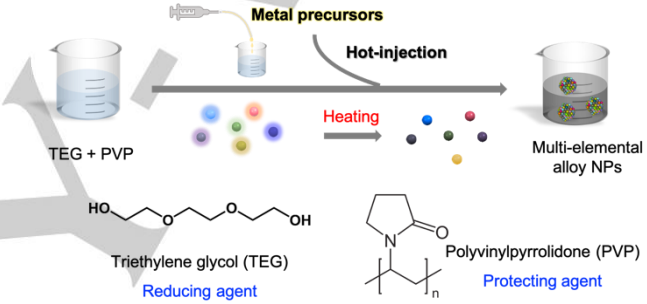

Figure 2. Schematic illustration of the hot-injection method.

3.1.1. Hot-injection Method

In 2020, Wu and coauthors reported the first example using a non-equilibrium wet-chemical process to synthesize HEA NPs.[54] As shown in Figure 2, the solution of the metal precursors was injected into a preheated mixture of reducing agent (i.e., triethylamine glycol, TEG) and protecting agent (i.e., polyvinylpyrrolidone, PVP). This was termed the hot-injection method, which ensures the reduction of all metal ions simultaneously.[73]

Taking IrPdPtRhRu HEA NPs as a showcase, five metal precursors, namely, H_2IrCl_6, $K_2[PdCl_4]$, $K_2[PtCl_4]$, $RhCl_3{\cdot}nH_2O$, and $RuCl_3{\cdot}nH_2O$, were dissolved in ultrapure water (0.2 mmol of each precursor, total 50 mL water).[57] Then, the aqueous solution was added dropwise to a preheated TEG solution (300 mL) containing PVP (K30, MW ca. 40000, 1.11 g) at 230°C. High-angle annular dark-field scanning transmission electron microscopy (HAADF-STEM) images showed that the prepared NPs had a mean diameter of 5.5 ± 1.2 nm. The energy-dispersive X-ray spectroscopy (EDX) maps showed the homogenous distribution of each element over the whole NP (Figure 3a). X-ray photoelectron spectroscopy (XPS, Mg $K\alpha$ anode) showed that each peak could be assigned a metallic state (Figure 4a,b). Furthermore, the lab XPS using Al or Mg $K\alpha$ was useful in determining the surface compositions. The consistent result between XPS (surface composition) and X-ray fluorescence

spectroscopy (XRF, bulk composition) (Figure 4c) suggested the successful preparation of HEA NPs by the hot-injection method.

A similar method can be used to synthesize PVP-protected platinum-group-metal (PGM) HEA NPs (PGM-HEA NPs, Figure 5a,b)[54] and noble-metal group HEA NPs (NM-HEA NPs, Figure 5c,d).[24] Both PGM-HEA NPs and NM-HEA NPs can be well-fitted with a single fcc phase.

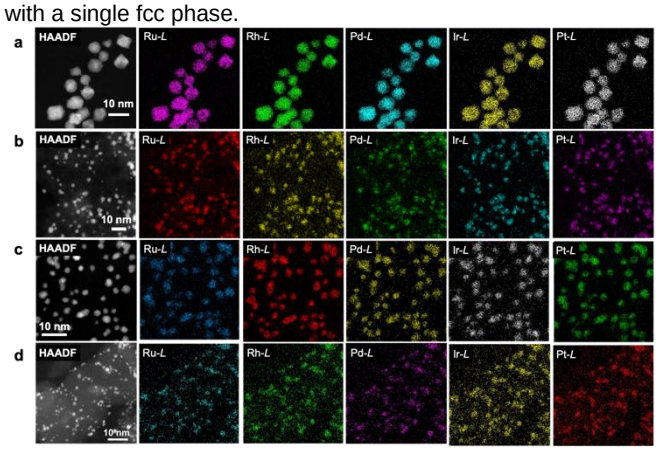

Figure 3. HAADF-STEM images and their EDX maps of IrPdPtRhRu HEA NPs prepared by different methods. Hot-injection method with (a) PVP as protecting agent (adapted with permission from ref. [57] Copyright 2020, The Royal Society of Chemistry) and (b) carbon as support (PVP-free) (adapted with permission from ref. [68] Copyright 2021, The Royal Society of Chemistry). Continuous-flow reactor method with (c) PVP as protecting agent (equipment in Figure 6a) (adapted with permission from ref. [69] Copyright 2021, American Chemical Society) and (d) carbon as support (PVP-free) (equipment in Figure 6c,d) (adapted with permission from ref. [70] Copyright 2022, American Chemical Society).

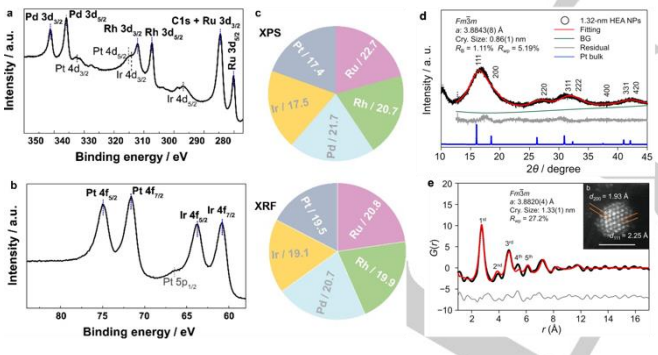

Figure 4. Core-level XPS spectra of IrPdPtRhRu HEA NPs in (a) 277–350 eV and (b) 55–88 eV. (c) Metallic ratios measured by XPS and XRF. Reprinted with permission from ref. [57] Copyright 2020, The Royal Society of Chemistry. (d) Synchrotron XRD pattern of 1.32-nm HEA NPs and its corresponding Rietveld refinement results. The black circles and red, green, and gray curves represent experimental data, fitting, background, and residual curves, respectively. Pt bulk data are represented by the blue curve. The X-ray radiation wavelength is 0.630327(7) Å. (e) PDF data and the fitting result of 1.32-nm HEA NPs. Experimental data, fitting, and residual curves are represented by the black circles and red and gray curves, respectively. The inset is the atomic-resolution HAADF-STEM image with 2-nm scale bar. Reprinted with permission from ref. [70] Copyright 2022, American Chemical Society.

PVP is a surface-protecting agent that might influence the catalytic process of HEA NPs.[74–76] In a modified process, Maruta et al. mixed the metal precursors with carbon support and obtained carbon-supported PVP-free HEA NPs.[68] As shown in Figure 3b, the mean diameter of the carbon-supported IrPdPtRhRu HEA NPs was 4.6 ± 1.7 nm. The homogenous distribution of each element could be confirmed from the EDX maps.

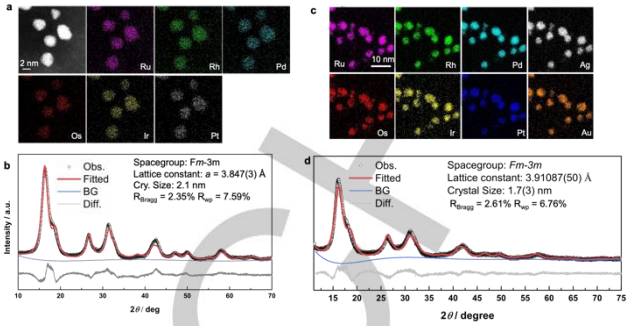

Figure 5. (a) HAADF-STEM images and corresponding EDX maps and (b) synchrotron XRD pattern and Rietveld refinement result of PGM-HEA NPs. Adapted with permission from ref. [54] Copyright 2020, American Chemical Society. (c) EDX maps and (b) synchrotron XRD pattern and Rietveld refinement result of NM-HEA NPs. Adapted with permission from ref. [24] Copyright 2022, American Chemical Society. EDX maps were obtained by *L*-line characteristic X-ray from each element. The radiation wavelength for the XRD of PGM-HEA NPs and NM-HEA NPs is 0.62938(6) and 0.63003(7) Å, respectively. The black circles are experimental data. The red, blue, and gray lines are background line, fitting data, and residual data, respectively

3.1.2. Continuous-flow Reactor Method

In contrast to batch synthesis, continuous-flow systems can be used to realize mass production easily because of the high reproducibility provided by the stable reaction conditions.[77–82] With the development of various types of flow-reactors, alloy NPs with different compositions and structures have been reported in the last 5 years.[69,70]

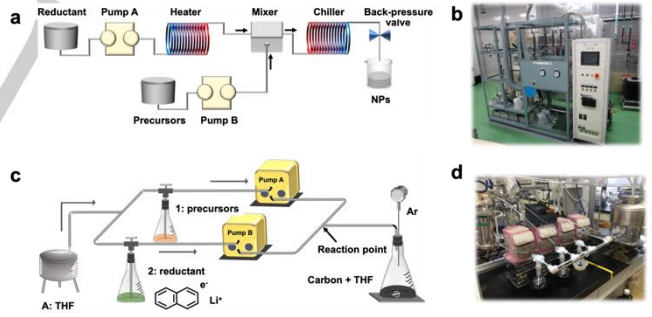

Figure 6. Schematic image (a,c) and real set-up image (b,d) of two home-designed flow-reactors. (a) is reprinted with permission from ref. [69] Copyright 2021, American Chemical Society. (c) is reprinted with permission from ref. [70] Copyright 2022, American Chemical Society.

Kusada et al. reported the first example of the synthesized HEA NPs by using a home-designed flow reactor.[69] Inspired by the hot-injection methods employed in the batch synthesis, the reactor was designed to be able to realize the concurrent supply of the constituent atoms during the nucleation and particle growth processes. Using the IrPdPtRhRu HEA NPs as an example, the flow reactor pumps reductant (50 vol% ethanol aqueous solution with NaOH) and metal precursors ($RuCl_3{\cdot}nH_2O$, $RhCl_3{\cdot}3H_2O$, $K_2[PdCl_4]$, $IrCl_4{\cdot}nH_2O$, $K_2[PtCl_4]$, and PVP in water) separately (Figure 6a, b). The reductant was preheated to 300°C, which ensured the simultaneous reduction of all the constituent ions

when they met the reductant in the mixer. A back-pressure valve was equipped with the reactor so that some solvents (and reductants) with low boiling points, such as ethanol, were heated to higher temperatures. In the current case, the back-pressure was set as 9.5 MPa. The mean diameter of the synthesized HEA NPs was 3.1 ± 0.3 nm (Figure 3c). STEM-EDX analysis showed that all five elements were homogeneously and randomly distributed in each NP.

Quite recently, Minamihara and coauthors developed a desktop-type flow reactor capable of synthesizing ultra-small HEA NPs.[70] The flow reactor has two diaphragm pumps with smooth pulsation to supply Solution 1 (mixture of acetylacetonate salts of Ir, Pd, Pt, Rh, and Ru dissolved in deoxidized tetrahydrofuran [THF]) and Solution 2 (lithium naphthalenide in THF) separately (Figure 6c,d). Two solvents were deoxidized and the reaction proceeded under Ar. After filling the whole line with THF pumped from tank A, Solutions 1 and 2 were simultaneously flowed at 21.0 mL/min. In only 15 seconds, the black solution appeared at the exit of the tube and dropped into the carbon-containing THF solution. As shown in Figure 3d, the HAADF-STEM image indicates that the obtained HEA NPs are homogeneously dispersed on carbon with an average diameter of 1.32 ± 0.41 nm. The elemental maps of Ir, Pd, Pt, Rh, and Pd corresponding to the HAADF-STEM image showed that all five of the elements are homogeneously distributed in the whole area of NPs. The XRD pattern of 1.32-nm HEA NPs shows broad peaks owing to the ultra-small particle size and lattice distortion caused by the mixing of multiple elements. Rietveld refinement suggests that the 1.32-nm HEA NPs is an fcc structure having a lattice constant of 3.8843(8) Å (Figure 4d). The pair distribution function (PDF) analysis using high-energy XRD data further suggests an fcc structure with a 3.8820(4) Å lattice parameter and 1.33(1)-nm particle size (Figure 4e). Moreover, the lattice distances (2.25 and 1.94 Å) given by the atomic-resolution HAADF-STEM (inset of Figure 4e) are consistent with the 2.24 and 1.94 Å distances calculated from the result of the PDF analysis.

3.1.3. Heating-up Method

In the heating-up method, all the metal precursors, reducing agents, protecting agents, and other additives are mixed first, generally at room temperature (RT). Then, the mixture is heated to a high temperature to ensure the reduction of metal ions.

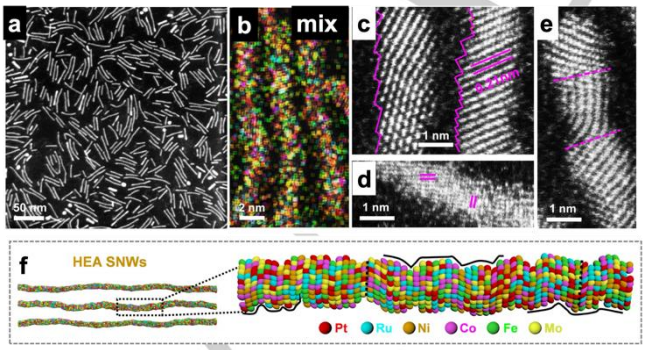

Figure 7. (a) HAADF-STEM image, (b) overlapped images of HAADF-STEM-EDX elemental maps, and (c-d) atomic-resolution STEM images, and (f) 3D atomic models of PrRuNiCoFeMo HEA SNWs. Reprinted with permission from ref. [28] Copyright 2021, Springer.

Li et al. synthesized $Pt_{18}Ni_{26}Fe_{15}Co_{14}Cu_{27}$ HEA NPs by a simple low-temperature oil-phase strategy.[30] All the metal acetylacetonate precursors were mixed with CTAC, glucose, and $Mo(CO)_6$ in OAm at RT. Then, the mixture was heated to 220°C at 5°C/min under 400 rpm-stirring for 2 h. The as-prepared $Pt_{18}Ni_{26}Fe_{15}Co_{14}Cu_{27}$ HEA NPs had an average size of 3.4 nm and were well-dispersed. XPS results showed that the Pt was mainly in zero-valence state, while the other 3D-elements existed in both zero-valance and oxidized states. An interesting point was that although $Mo(CO)_6$ was used in the synthesis, it worked as a reducing agent, and Mo was absent in the final product. In another study, Zhan and coauthors synthesized PtRuNiCoFeMo HEA subnanometer nanowires (SNWs) through a similar process by using $Mo(CO)_6$ as a precursor.[28] The acetylacetonate salts of Pt, Ru, Ni, Co, and Fe, together with $Mo(CO)_6$, glucose, and stearyl trimethyl ammonium bromide (STAB), were dissolved in OAm. After heating at 210°C for 5 h in an oil bath, PtRuNiCoFeMo HEA SNWs were synthesized. Interestingly, under similar conditions to those of HEA SNWs, except for the addition of STAB and glucose, HEA NPs could be obtained. The obtained HEA SNWs had a diameter of 1.8 ± 0.3 nm (Figure 7a) and an fcc structure with a smaller lattice constant compared with pure Pt. HAADF-STEM-EDX elemental maps showed the uniform distribution of all metals in the HEA SNWs (Figure 7b). The aberration-corrected high-resolution STEM (HRSTEM) images show abundant atomic steps and defect-rich lattice mismatch in the obtained HEA SNW (Figure 7c,d). A 3D atomic model of HEA SNWs (Figure 7f) revealed numerous facet boundaries and plentiful surface atomic steps.

Zhang and coauthors also reported a similar process to synthesize PdFeCoNiCu HEA NPs.[65] Namely, all the metal precursors were dissolved in OAm, and the mixture was heated from RT to 220°C and maintained at 220°C for 2 h. The prepared HEA NPs were well-dispersed with an average diameter of 34 nm and with a metal ratio of Pd/Fe/Co/Ni/Cu = 19:21:20:22:17. The XRD results suggested a body-centered cubic structure. The EDX maps showed a relatively homogenous distribution of Pd, Fe, Co, Ni, and Cu over the whole NPs.

3.1.4. Other Methods

By using a facile one-step, high-intensity ultrasound irradiation process, Okejiri and coauthors found that single-phase HEA (AuPdPtRhRu) nanocrystals could be obtained by co-reducing Au^{3+}, Pd^{2+}, Pt^{2+}, Rh^{3+}, and Ru^{3+} with alcoholic ionic liquid (AIL).[67] After mixing the metal precursors and carbon in AIL, the mixture was submitted to sonication (20 kHz,10 min); no external heat-treatment process was needed in this method (Figure 8a). The control group showed that non-AIL failed to form single-phase HEA nanocrystals. The hydroxyl functionality of AIL was key to ensuring the formation of single-phase HEA nanocrystals in a one-pot reaction.[83–85] As shown in Figure 8b, the as-obtained nanocrystals are composed of homogenously distributed elements of Au, Pd, Pt, Rh, and Ru, as expected.

Chen et al. presented a two-step process to prepare monodisperse HEA NPs (Figure 8c).[58] First, intermetallic monodispersed PdCu B2 seeds were prepared. Then, the core@shell PdCu B2@PtNiCo NPs were synthesized by depositing Pt, Ni, and Co on the intermetallic PdCu B2 seeds using a seed-mediated co-reduction process (Figure 8d,e). These core@shell NPs were then loaded on carbon and further annealed to facilitate interdiffusion and PdCuPtNiCo HEA

formation. By using this method, the authors obtained well-dispersed NPs on carbon (Figure 8f,g).

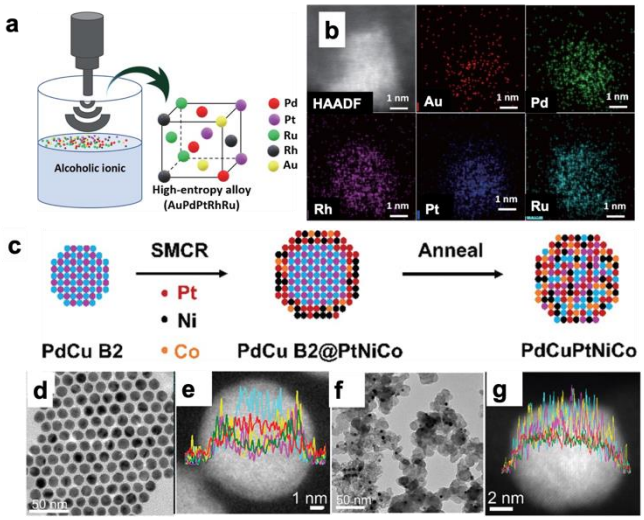

Figure 8. (a) Schematic illustration of the ultrasound-driven wet chemistry method using an AIL to synthesize HEA nanocatalysts. (b) HAADF image and EDX elemental maps of the AuPdPtRhRu-NPs/C. Reprinted with permission from ref. [67] Copyright 2021, Springer. (c) Scheme of the synthetic process of PdCuPtNiCo HEAs. SMCR: seed-mediated co-reduction. (d) TEM bright-field image and (e) line scan profile of PdCu B2@PtNiCo. (f) TEM bright-field image and (g) line scan profile of carbon-supported PdCuPtNiCo HEAs. Reprinted with permission from ref. [58] Copyright 2021, The Royal Society of Chemistry.

Feng et al. synthesized a series of ultra-small HEA NPs from quinary NiCoFePtRh to octonary FeCoNiCuCdPtIrPd by using a two-step method.[62] The metal salts were dissolved in an H_2SO_4 solution in an Ar-filled box. Next, Ketjen black carbon was added to the solution of the precursors and the mixture was stirred to ensure uniform dispersion. The mixture was first reduced with a $NaBH_4$ aqueous solution. After 8 h of stirring, a dried powder was obtained by centrifugation, washing, and drying sequence. Finally, ultra-small HEA/C NPs were obtained by annealing/reducing the powder under flowing Ar at 350°C for 3 h. In this study, the authors claimed that adding Ketjen black carbon before $NaBH_4$ and restricting the loading amount of metals below 5 wt.% were key parameters to obtaining ultra-small HEA NPs.

Wang and coauthors synthesized hollow multiple noble metallic nanoalloys (AuHgPdPt) by Hg-assisted galvanic replacement reaction.[66] First, hollow Au NPs were prepared. Next, the Hg was introduced to form AuHg hollow nanoalloys. Then, with the addition of Pd and Pt salt, the Hg atoms were replaced with the Pt and or Pd atoms because of the higher reduction potential of Pt(IV)/Pt(0) and Pd(II)/Pd(0) compared with Hg(II)/Hg(0).

3.2. Electronic Structure of Multi-element Alloy NPs

The electronic structure determines the properties of solid materials. In monometals and binary alloys, the configurations of neighboring atoms are easy to determine; therefore, their properties can be understood and predicted by using the electronic structures of the principal elements experimentally and theoretically (i.e., *d*-band theory).[86–88] In HEA NPs, every atom is distinct because of the different configurations of neighboring atoms. Therefore, revealing or predicting the properties of HEA NPs requires an understanding of the local electronic structure of atoms both experimentally and theoretically.

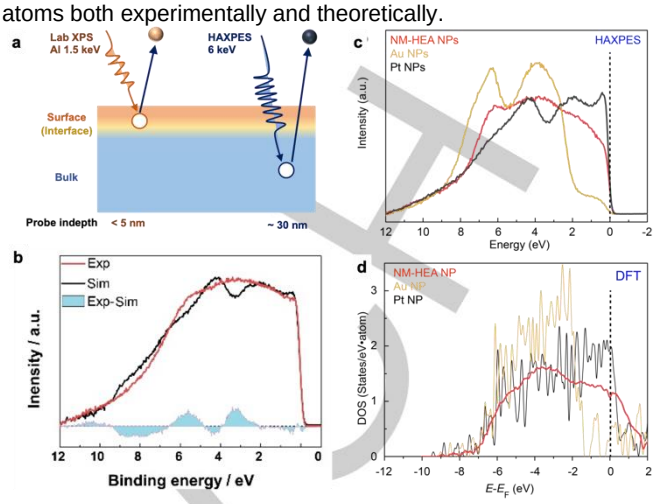

Figure 9. (a) Schematic illustration of lab XPS and HAXPES. The solid spheres represent electrons and the hollow spheres indicate holes after the escape of electrons. (b) VB spectrum (red line) of IrPdPtRhRu HEA NPs and the simulation spectrum (black line) obtained by the linear combination of the VB spectra of monometallic NPs. Reprinted with permission from ref. [57] Copyright 2020, The Royal Society of Chemistry. (c) Experimental VB spectra and (d) DOS calculated by DFT of NM-HEA NPs, Pt NPs and Au NPs. Reprinted with permission from ref. [24] Copyright 2022, American Chemical Society.

To understand the electronic structure of HEA NPs, we focus on the valence band (VB) structure, which significantly influences the catalytic properties of NPs. For example, from the VB spectroscopy, we can calculate the d-band center and predict the catalytic properties of NPs. In 2020, Wu and coauthors first revealed the VB features of HEA NPs by hard X-ray photoelectron spectroscopy (HAXPES, photon energy of 5.95 keV).[57] As shown in Figure 9a, the lab source XPS typically used Al or Mg $K\alpha$ anode with a probe depth of several nanometers; namely, from the surface to interface region. HAXPES uses higher X-ray energy and can thus achieve a longer probe depth (ca. 30 nm). Therefore, for NPs with a size below 10 nm, HAXPES can be used to reveal the bulk information of all atoms. Figure 9b shows the VB spectrum of IrPdPtRhRu HEA NPs, the linear combination of the VB spectra of the monometallic NPs that represent a physical mixture of the five elements, and their difference spectra marked in cyan regions. Such differences suggest that the orbitals of the constituents in HEA NPs hybrids with each other; i.e., the formation of solid-solution alloys. Interestingly, the VB spectrum of IrPdPtRhRu HEA NPs does not have any obvious peaks, which is distinct from the VB of monometallic NPs having clear peaks. A similar featureless VB spectrum was found in the case of NM-HEA NPs (Figure 9c).[24] The authors concluded that the “featureless” VB spectrum may be a common feature of HEA caused by countless types of local electronic structures, which was further verified by DFT with NP models composed of 201 atoms in follow-up research.

Similar to the experimental VB spectrum, the calculated density of states (DOS) profile of NM-HEA NP is more “featureless” and smoother than those of monometals (Figure 9d).[24] Both experimental VB spectra and DFT calculations confirmed that there are numerous atomic configurations and distinct local DOS (LDOS) profiles in HEA NPs. The authors further analyzed the LDOS of every surface atom in the

monometallic NPs and NM-HEA NP. Figure 10a shows that the *d*-band center value (ε_d) distribution of the atoms of each element in NM-HEA NPs is wider than that of monometallic NPs.[24]

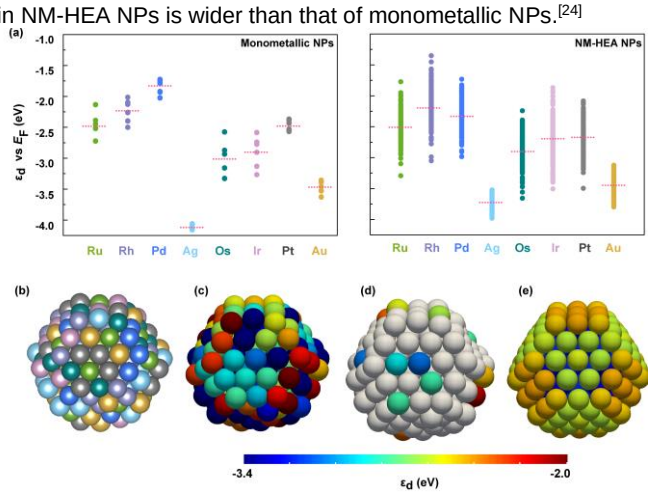

Figure 10. *d*-band center values of the surface atoms in (a) monometallic NPs and NM-HEA NPs. The pink dashed line is the average *d*-band center of each element. (b) DFT model of NM-HEA NPs. Illustration of the *d*-band center of every surface atom in (c) NM-HEA NPs and (e) monometallic Pt NPs. In (d), only the *d*-band center of surface Pt atoms in NM-HEA NPs are shown. All other atoms are shown in gray. Reprinted with permission from ref. [24] Copyright 2022, American Chemical Society.

Particularly, monometallic Au and Ag have more negative values than the other elements, which would be also an intrinsic reason for the inert nature of Au and Ag during catalysis. While some Au and Ag atoms have ε_d values that are similar to some Ir, Ru, Pt, and Os atoms in NM-HEA NPs, as shown in Figure 10c, the ε_d values of the surface atoms in the NM-HEA (DFT model in Figure 10b) range from –3.4 to –2.0 eV. The different color shown in Figure 10d indicates that the ε_d of surface Pt atoms was different in NM-HEA NPs. By contrast, in the same facets of monometallic Pt NPs, the surface Pt atoms have similar ε_d (Figure 10e). In addition, through plotting the LDOS profiles in HEA NPs, some atoms from the same element have different LDOS profiles, whereas atoms from different elements have similar LDOS profiles. That is, one atom in HEA loses its elemental identity. It is possible to create an ideal LDOS by adjusting the neighboring atoms. As a demonstration, we showed that the HER activity of NM-HEA NPs is much higher than the IrPdPtRhRu HEA NPs, although Au, Ag, and Os have ignorable HER activities. As shown in Figure 10, Au, Ag, and Os possess suitable LDOS which might work as an active center for HER. Meanwhile, these “inert” atoms may make the other atoms more active by forming a suitable configuration for HER.

3.3. Properties of Multi-element Alloy NPs

3.3.1. Electrocatalytic Reactions

To date, HEA NPs have been extensively used as catalysts for a wide range of electrocatalytic reactions, such as hydrogen evolution reaction (HER),[24,30,53,57,62,65,66,68,70] hydrogen oxidation reaction (HOR),[28] oxygen reduction reaction (ORR),[58] methanol oxidation reaction (MOR),[30] ethanol oxidation reaction (EOR),[24] and nitrogen reduction reaction.[64]

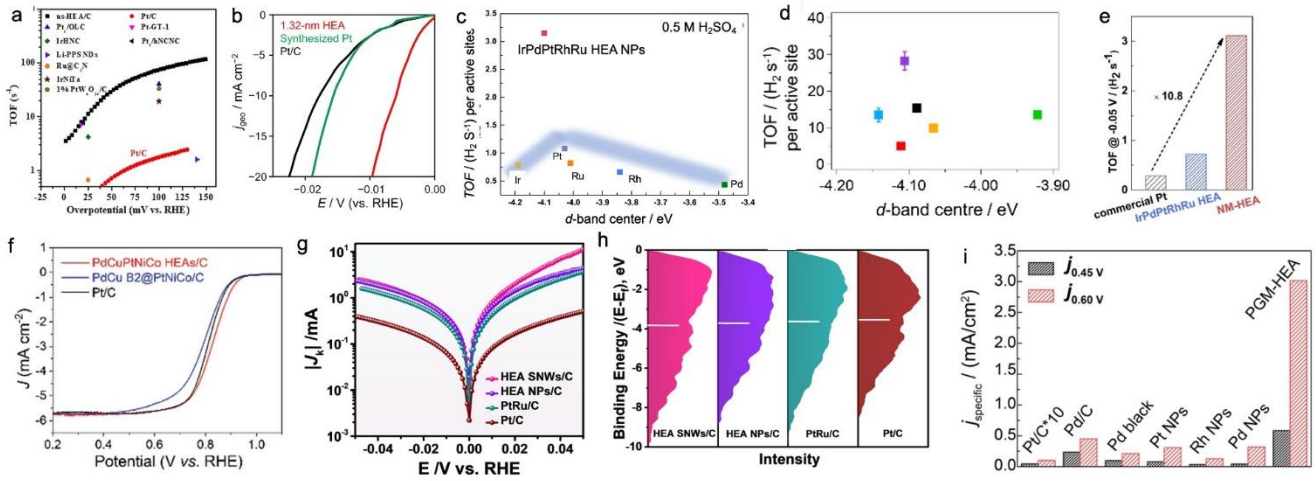

Figure 11. (a) TOF values of HER over us-HEA/C and other reported catalysts in 0.5 M H_2SO_4. Reprinted with permission from ref. [62] Copyright 2022, American Chemical Society. (b) Geometric activity of 1.32-nm HEA NPs, synthetic Pt, and commercial Pt/C in 1.0 M $HClO_4$. Reprinted with permission from ref. [70] Copyright 2022, American Chemical Society. (c) TOF values of HER of IrPdPtRhRu HEA NPs and monometallic NPs as a function of *d*-band center value in 0.05 M H_2SO_4. Reprinted with permission from ref. [57] Copyright 2020, The Royal Society of Chemistry. (d) TOF of HER of IrPdPtRhRu multi-element NPs with different ratios as a function of *d*-band center value in 1.0 M $HClO_4$. Adapted with permission from ref. [68] Copyright 2022, The Royal Society of Chemistry. (e) Comparing TOF values of HER over commercial Pt/C, IrPdPtRhRu HEA NPs, and NM-HEA NPs in 0.15 M H_2SO_4. Reprinted with permission from ref. [24] Copyright 2022, American Chemical Society. (f) ORR performance of PdCuPtNiCo HEAs/C in 0.1 M KOH. Reprinted with permission from ref. [58] Copyright 2021, The Royal Society of Chemistry. (g) Exchange current of HOR over HEA SNWs/C and the control group catalysts and (h) the corresponding VB spectra. Reprinted with permission from ref. [28] Copyright 2021, Springer. (i) Specific current densities of monometals and PGM-HEA NPs for EOR.

Feng and coauthors reported that ultra-small NiCoFePtRh HEA/C showed a higher turnover frequency (TOF) of HER than did monometals and some reported catalysts tested under similar conditions (Figure 11a).[62] Operando X-ray absorption spectroscopy at each element and DFT calculations suggested that Rh and Pt are the reaction center for HER, and that the Pt showed weaker adsorption to H in the HEA matrix compared with the other elements. Minamihara et al.[70] also reported that 1.32-nm HEA showed higher HER activity than did monometallic Pt and commercial Pt/C (Figure 11b). Wu and coauthors tested the TOF values of IrPdPtRhRu HEA NPs and monometallic NPs, and further plotted the TOF values as a function of the *d*-band center that was calculated from the experimental VB spectrum.[57] They found that the HEA NPs had a very high TOF value that was out of the range in which *d*-band center theory works (Figure 11c). Maruta et al.[68] prepared IrPdPtRhRu multi-element NPs with different compositions. Although the lattice constant of the IrPdPtRhRu multi-element NPs follows Vegard's law, TOF values are not linearly correlated to the *d*-band center values (Figure 11d). In particular, they found that Pt-rich multi-element NPs have higher HER activity than do equal-ratio IrPdPtRhRu HEA NPs. In Wu and Maruta's works, they concluded that the *d*-band theory in monometals and binary alloys is valid because most surface atoms have similar local electronic structures, and therefore, the *d*-band center obtained from HAXPES can be used to understand or predict the tendency. For HEA NPs, LDOS are required to understand such nonlinear relationships because almost every atom is distinct. As a demonstration, the authors showed that NM-HEA NPs have much higher HER activity than do IrPdPtRhRu NPs, although Au, Ag, and Os have no HER activity at all (Figure 11e).[24] Wu et al. proposed that the LDOS of Au, Ag, and Os might be suitable for HER in the HEA matrix.

Chen and coauthors found that PdCuPtNiCo HEAs/C has higher ORR activity than do both PdCu B2@PtNiCo/C and commercial Pt/C in 0.1 M KOH (Figure 11f).[58] However, they note that in 0.1 M $HClO_4$, commercial Pt/C is the best among these three catalysts. The authors found that PdCuPtNiCo HEAs/C showed very high ECSA (79.4 $m^2\ g_{Pt}^{-1}$ for acid medium; 79.9 $m^2\ g_{Pt}^{-1}$ for alkaline medium) independent of electrolyte, whereas PdCu B2@PtNiCo/C had a smaller electrochemically active surface area (ECSA, 39.7 $m^2\ g_{Pt}^{-1}$ for acid medium; 43.8 $m^2\ g_{Pt}^{-1}$ for alkaline medium). As for commercial Pt/C, its ECSA is large (76.7 $m^2\ g_{Pt}^{-1}$) in 0.1 M $HClO_4$, but low in 0.1 M KOH (55.3 $m^2\ g_{Pt}^{-1}$).

Zhan and coauthors reported that PtRuNiCoFeMo HEA SNWs are highly active catalysts for HOR, having an exchange current value of 1.26 mA, which is 1.5, 2.4, and 4.5 times that of HEA NPs/C, PtRu/C, and Pt/C (Figure 11g).[28] The HEA SNWs/C has the deepest *d*-band center among the tested catalysts, which weakens the adsorption of H, but facilitates the adsorption of OH intermediate, as the author claimed (Figure 11h). DFT calculations also revealed that the enhanced HOR activity can be ascribed to the strong interactions between different metal sites, which can tune the binding strength of proton and hydroxyl.

Wu et al.[54] assumed that the multiple sites in HEA NPs could effectively catalyze complex reactions. As a demonstration, PGM-HEA NPs showed high activity toward 12-electron/proton reaction; i.e., the ethanol oxidation reaction. They found that PGM-HEA NPs can break the C–C bond at a very low potential.

3.3.2. Other Reactions

Okejiri and coauthors[67] reported that carbon-supported AuPdPtRhRu HEA NPs were a superior catalyst for selective hydrogenation of phenol to cyclohexanone. Moreover, HEA NPs/C can maintain high yield and selectivity over 95% for five usage cycles, demonstrating the excellent stability of the system.

4. Chemical Synthesis and Properties of Multi-element Ceramic NPs

Multi-element ceramics (or compounds) including HECs have also been eagerly investigated in the search for novel materials since Rost and coauthors reported the first example of bulk high-entropy oxides (HEOs) in 2015.[89] As with HEA, HECs also consist of more than five elements in a single phase, which provides large configurational entropy.[90] HECs can also be useful functional materials, not only as catalysts, but also, for example, as thermoelectric materials and ionic conductors, because unlike metallic HEAs, HECs are generally insulators or semiconductors.[91–93] Therefore, multi-element ceramic NPs including HEC NPs have also been studied since the first report of spinel-type (Co, Cu, Fe, Mn, Ni)$_3O_4$ NPs by Wang et al.[38]

Although there are fewer reports on multi-element ceramic NPs than on alloy NPs, multi-element ceramic NPs are also generally synthesized at higher temperatures to take advantage of their large configurational entropy. Their unique structure and properties including ionic conductivity and catalytic activity are nicely summarized in some reports.[94–96] Here, we introduce the synthesis and properties of multi-element ceramic NPs synthesized by solution-based chemical methods.

4.1. Oxide NPs

As far as we know, the first example of HEC NPs is spinel-type (Co, Cu, Fe, Mn, Ni)$_3O_4$ reported by Wang and coauthors in 2019.[38] The reported synthesis methods of bulk HEOs, such as nebulized spray pyrolysis process, flame spray pyrolysis, solid-phase sintering methods, and reverse co-precipitation processes, require high reaction temperature (more than 1000°C), which significantly accelerates particle growth.[97,98] Wang et al. succeeded in synthesizing HEO NPs at a low temperature. They first prepared a mixture of polyethylene oxide–polypropylene oxide–polyethylene oxide (PEO_{20}–PPO_{70}–PEO_{20}, Pluronic P123) as a surfactant, EG as a co-surfactant, and water. Then, $Co(Ac)_2{\cdot}4H_2O$, $Ni(Ac)_2{\cdot}4H_2O$, $Mn(Ac)_2{\cdot}4H_2O$, $Fe(Ac)_2$, $Cu(Ac)_2{\cdot}H_2O$, and hexamethylenetetramine were mixed in the solution and heated in an autoclave at 170°C for 15 h. Hexamethylenetetramine is considered to play two important roles. One is complete condensation and crystallization in the solvothermal reaction, and the other is a reduction in the pyrolysis temperature of the precursors during synthesis. Thanks to hexamethylenetetramine, five cations can disperse uniformly in the product of the hydrothermal synthesis. After the product was washed and dried, the product was calcined at 400°C for 2 h to obtain the HEO NPs. The authors chose five elements—Co, Cu, Fe, Mn, and Ni—as constituents because their atomic radii are similar and they are miscible with each other in binary and ternary systems.[99]

The XRD pattern of the obtained powder (Figure 12b; red curve) indicated a spinel structure ($Fd\bar{3}m$) with all five elements, as shown in Figure 12a. As a control experiment, the authors also

prepared a bulk spinel oxide (Figure 12b; black curve) by the traditional reversible co-precipitation method, where the oxide is synthesized by calcination (1000°C for 1 h) of the precipitate obtained by mixing the precursors in alkaline solution. The element maps of the spinel NPs indicated the homogeneous distribution of five metal elements in the particles (Figure 12c). Furthermore, high-resolution TEM images revealed that the average particle size was approximately 5 nm. These results showed that this method can be used to synthesize nanometer-sized HEO, which are much smaller than the HEO prepared by conventional methods. The authors concluded that the use of Pluronic P123 and EG as surfactants could realize the synthesis of stable nanometer-sized HEO. The authors utilized HEO NPs as an electrochemical catalyst for oxygen evolution reaction (OER) in 1M KOH for the first time. The HEO NPs were loaded on O_2 plasma-treated carbon nanotubes to improve conductivity. This catalyst showed higher OER activity than did mixed metal oxides with fewer elements. The authors concluded that the diversity of chemical elements and their valence states in the HEO generates many intermediates, which can overcome the kinetic barrier more easily than can the other catalysts with fewer elements.

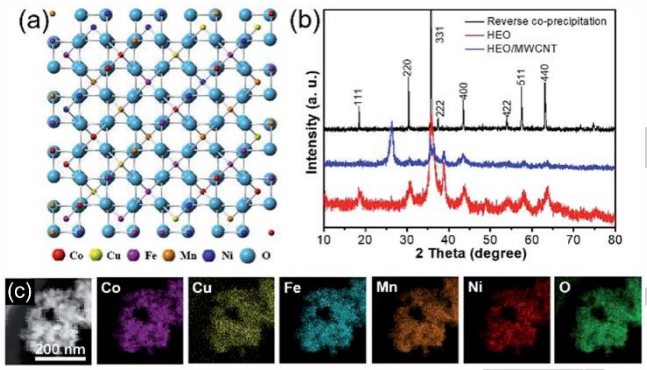

Figure 12. (a) Model of the crystal structure, (b) XRD patterns (Cu Kα), and (c) EDX elemental mapping images of spinel-type (Co, Cu, Fe, Mn, Ni)$_3O_4$ NPs. ref. [38] Copyright 2019, The Royal Society of Chemistry.

Ting[55,100] and Chang et al.[55,100] also reported spinel-type (Cr, Mn, Fe, Co, Ni)$_3O_4$ HEO NPs prepared by similar methods for use as a noble anode material in a lithium-ion battery. $Cr(NO_3)_3{\cdot}9H_2O$, $Mn(NO_3)_2{\cdot}6H_2O$, $Fe(NO_3)_3{\cdot}9H_2O$, $Co(NO_3)_2{\cdot}6H_2O$, and $Ni(NO_3)_2{\cdot}6H_2O$ were dissolved in water, and then (1-hexadecyl)trimethylammonium bromide (CTAB) was added to the solution. The solution was transferred into an autoclave after the addition of urea for hydrothermal treatment at 140°C for 5 h. The precipitate after the hydrothermal reaction was washed and dried, and then calcined in air at 900°C for 2 h. The obtained powder after the calcination was found to be single-phase spinel-type NPs with an average diameter of approximately 100–200 nm. STEM-EDX analysis revealed that the five metal elements were homogeneously distributed in a particle. On the other hand, the as-prepared sample without calcination showed a different XRD pattern from the calcined sample, indicating the formation of metal hydroxycarbonate and carbonate. A conceivable formation mechanism of the HEO NPs is shown in Figure 13. In this synthesis, CTAB was used as the surfactant (Figure 13a). Two paths (Paths I and II in Figure 13b) are considered to be followed in the solution to form a complex of metal ions and CTAB. In Path I, CTAB forms micelles and catches individual metal ions on the surface. This type of unit is stabilized by the OH^- and CO_3^{2-} produced from the hydrolysis of urea. In Path II, metal ions are captured and shared by several CTAB monomers. Subsequently, hydroxycarbonate and carbonate compounds form during the hydrothermal treatment because of the reactions among the metal ions, OH^-, and CO_3^{2-}. The compounds show NP and nanosheet morphologies derived from Paths I and II, respectively (Figure 13c). Finally, after heat treatment at 900°C, single-phase spinel-type HEO NPs are obtained (Figure 13d). The authors used these spinel-type HEO NPs as Li-ion conductors because the spinel structure has unique 3D Li^+ conducting pathways and a rock-salt-type HEO with oxygen vacancies, and the material showed very high Li^+ ion conductivity.[101] The obtained spinel-type HEO NPs showed an extraordinary charge–discharge capacity of 1235 mA h g^{-1}, high cycling stability, and fast Li^+ transport.

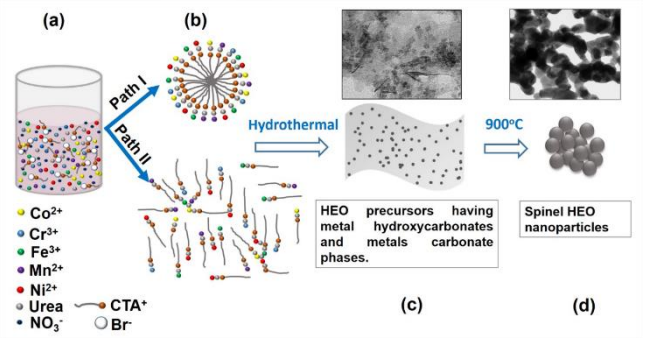

Figure 13. Formation mechanism of (Co, Cr, Fe, Mn, Ni)$_3O_4$ NPs. (a) precursor solution, (b) two paths to form complex in the solution, (c) the formation of hydroxycarbonate and carbonate compounds during the hydrothermal treatment, (d) HEO NPs after heating. ref. [55] Copyright 2020, The Royal Society of Chemistry.

Kheradmandfard et al.[61] synthesized rock salt-type (Mg, Cu, Ni, Co, Zn)O NPs by applying a microwave-assisted method. The precursor solution was prepared by mixing pH-adjusted $Mg(NO_3)_2{\cdot}6H_2O$, $Cu(NO_3)_2{\cdot}3H_2O$, $Ni(NO_3)_2{\cdot}6H_2O$, $Co(NO_3)_2{\cdot}6H_2O$, and $Zn(NO_3)_2{\cdot}6H_2O$ solutions and exposed to microwave irradiation for 3 min in ambient air. The precipitate was washed and dried. Although the as-prepared powder showed no sharp XRD peaks reflecting an amorphous or nanocrystalline structure, the powder calcined at more than 370°C showed a clear rock salt-type XRD pattern. The crystallite size became bigger with increasing calcination temperature. The authors claimed that microwave irradiation provides two interactions—dipole rotation and ionic conduction—that accelerate the collisions of metal cations and the nucleation of amorphous HEO particles. Therefore, the reaction time of HEO can be significantly decreased by microwave irradiation from hours to minutes and seconds.

Most of the reports adopt calcination to obtain oxide NPs; however, calcination promotes particle aggregation and growth that is not suitable for the fabrication of very small NPs with a high surface area. Okejiri et al.[56] synthesized perovskite-type $BaZrO_3$ and its high-entropy analogues with an average crystallite size of about 5.9 nm through an ultrasonication-based method at RT

(Figure 14a). Sonochemical synthesis is a unique technique that utilizes an acoustic cavitation phenomenon caused by high-intensity ultrasound irradiation. This phenomenon can be expressed as the formation, continual growth, and implosive collapse of micro-bubbles in solution, which provides huge energy in the micro-region with very high temperatures above 5000°C and high pressures over 2000 atm within 10^{-9} s.[72] For the synthesis of eight elements $Ru_{0.13}/Ba_{0.3}Sr_{0.3}Bi_{0.4}(Zr_{0.2}Hf_{0.2}Ti_{0.2}Fe_{0.27})O_3$ (Ru/HEPO-7), $BaCl_2 \cdot 2H_2O$, $SrCl_2 \cdot 6H_2O$, $Bi(NO_3)_3 \cdot xH_2O$, $ZrCl_4$, and $HfCl_4$ were mixed and dissolved in $TiCl_4$ solution. $Fe(NO_3)_3 \cdot 9H_2O$ and $RuCl_3$ were dissolved in water. These solutions were added to a 20.0 M NaOH solution where the ultrasonication equipment was set. The mixed solution was exposed to ultrasonic irradiation by directimmersion of an ultrasonic titanium horn operating at 20 kHz about for 10 min. After the sonication, the resulting precipitate was separated, washed with water, and dried at 80°C for 3 h to obtain the final crystallite. The obtained powders showed clear XRD patterns indicating the perovskite structure with *Pm*3*m* space group similar to perovskite-type $BaZrO_3$ (Figure 14b). The crystallite size was calculated to be 5.9 nm from the broad XRD peaks by Scherrer's equation. The EDX elemental maps of Ru/HEPO-7 are shown in Figure 14c. The diameter of the particle is around 80 nm, and all eight elements are homogeneously distributed in the particle. These results demonstrated that the sonochemical-based method is a simple way to synthesize HEO NPs without calcination. Okejiri et al. investigated the CO catalytic activity of HEO NPs. They compared the catalytic activity of Ru/HEPO-7 with those of $BaRuO_3$ and $Ba_{0.4}Sr_{0.4}Bi_{0.2}(Zr_{0.3}Hf_{0.3}Ti_{0.2}Fe_{0.2})O_3$ (HEPO-7). Ru/HEPO-7, containing only 0.2 wt% of Ru, reached 50% CO conversion at 90°C, whereas $BaRuO_3$, containing 53 wt% of Ru, reached 50% CO conversion at around 255°C, and HEPO-7, without Ru, did not reach CO conversion until 300°C. The authors concluded that the superior catalytic activity of Ru/HEPO-7 NPs could be derived from the good dispersion of Ru in the high-entropy phase.

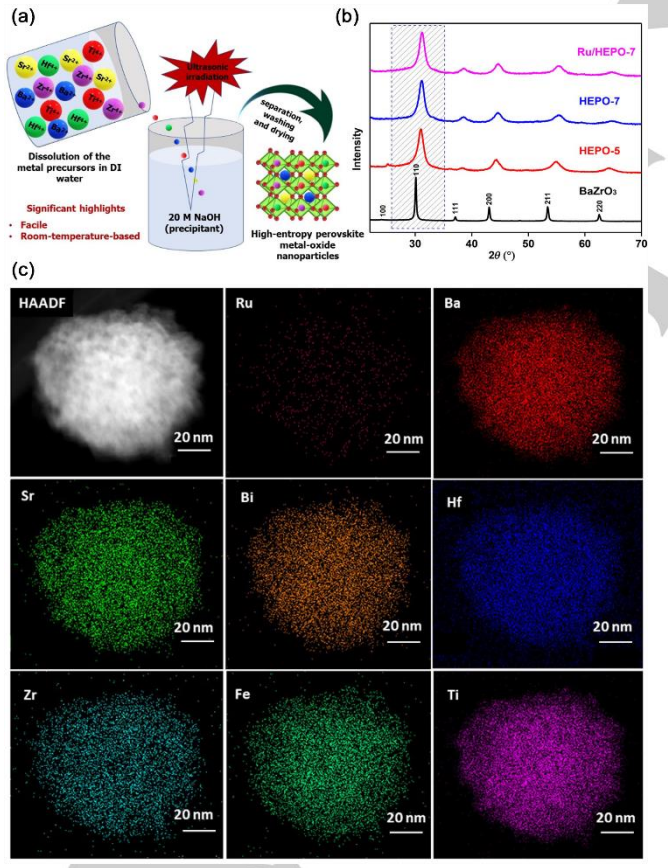

Figure 14. (a) Schematic of sonochemical-based synthesis of HEO NPs. (b) XRD patterns of $BaZrO_3$, HEPO-5, 7, and Ru/HEPO-7. (c) EDX elemental maps of Ru/BaSrBi(ZrHfTiFe)O_3 (Ru/HEPO-7). ref. [56] Copyright 2020, Wiley-VCH Verlag GmbH & Co. KGaA.

4.2. Other NPs

Although the most common multi-element materials are alloys and oxides, some multi-element carbides, nitrides, diborides fluorides, and chalcogenides have also been reported.[36,102–106] They are also typically obtained at high temperatures to take advantage of large configurational entropy. Nevertheless, there are still a few studies reporting on chemical synthesis at low temperatures. McCormick et al.[59] synthesized wurtzite-type $Zn_{0.25}Co_{0.22}Cu_{0.28}In_{0.16}Ga_{0.11}S$ NPs by simultaneous multi-cation exchange from roxbyite $Cu_{1.8}S$ NPs (Figure 15a). Zn, Co, In, and Ga chlorides were dissolved in a mixture of oleylamine, octadecene, and benzyl ether and heated under Ar to form a cation-oleylamine complex. $Cu_{1.8}S$ NPs were dissolved in

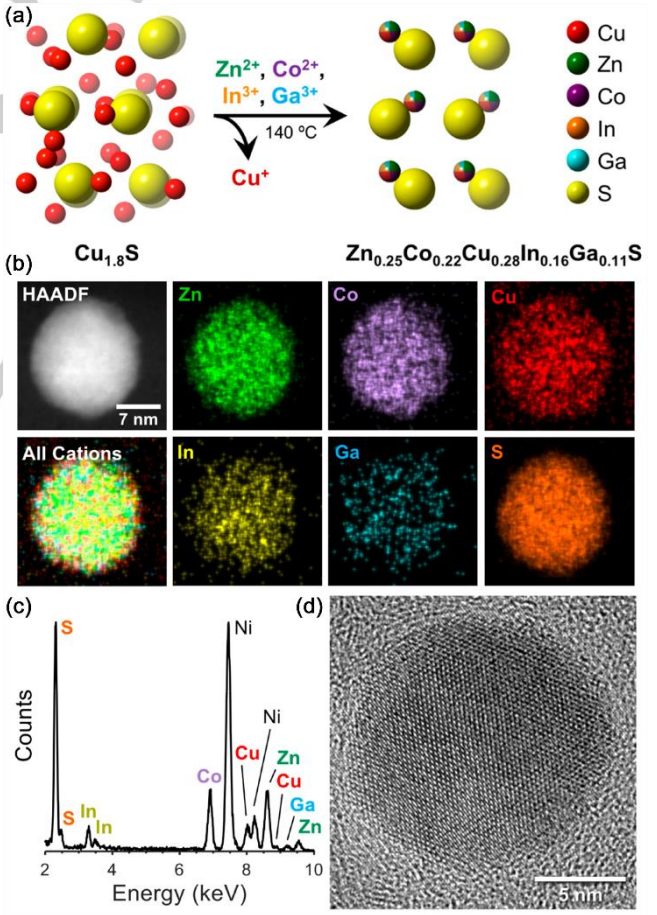

Figure 15. (a) Schematic of the formation of $Zn_{0.25}Co_{0.22}Cu_{0.28}In_{0.16}Ga_{0.11}S$ NPs. (b) HAADF-STEM image and EDX elemental maps, (c) EDX spectrum, and (c) HRTEM image of $Zn_{0.25}Co_{0.22}Cu_{0.28}In_{0.16}Ga_{0.11}S$ NPs. The Ni signal in (c) is from the TEM grid. (d) HRTEM image. Ref. [59] Copyright 2021, American Chemical Society.

trioctylphosphine (TOP) under Ar and rapidly injected into the cation solution at 140°C. After the reaction was held for 30 min at 140°C, the solution was cooled in an ice bath, and the NPs were obtained. It is known that cation exchange in nanocrystals is mainly determined by enthalpic factors. A soft base, for instance, TOP in a solution, coordinates with a soft acid, Cu^+, and accelerates the dissolution of Cu^+ from the crystal into the solution. This promotes the incorporation of harder acids (divalent and trivalent cations) in solution into the nanocrystal.[107] The product of Co^{2+}, Zn^{2+}, Ga^{3+}, and In^{3+} exchange of roxbyite $Cu_{1.8}S$ after the release of two Cu^+ are wurtzite CoS, ZnS, $CuGaS_2$, and $CuInS_2$, respectively (Figure 15a).[108–110] A HAADF-STEM image and corresponding EDX elemental maps and spectrum show that five cations and S are homogeneously distributed in one particle (Figure 15b,c). The particle of $Zn_{0.25}Co_{0.22}Cu_{0.28}In_{0.16}Ga_{0.11}S$ kept the single-crystalline nature of $Cu_{1.8}S$ NPs even after the cation exchange reaction (Figure 15d).

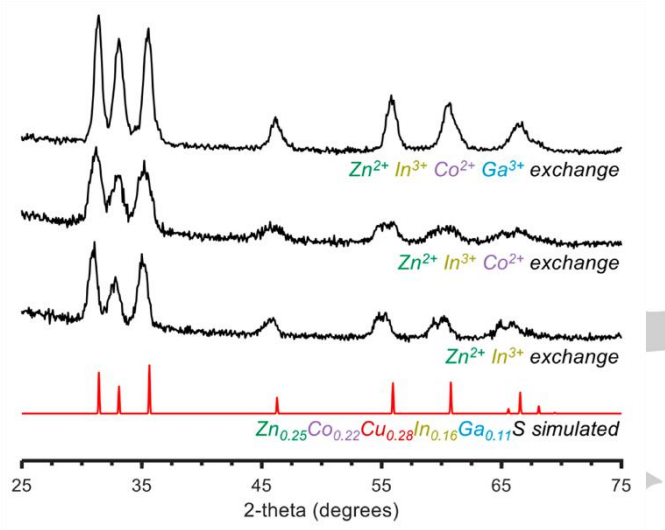

Figure 16. XRD patterns of cation exchanged sulfide NPs with different numbers of cations (λ = Co *K*α) and simulated pattern of $Zn_{0.25}Co_{0.22}Cu_{0.28}In_{0.16}Ga_{0.11}S$. Ref. [59] Copyright 2021, American Chemical Society.

To investigate the entropic contribution to the formation of multi-element sulfide NPs, the authors synthesized 3- and 4-cation systems (Zn^{2+}, In^{3+}, Cu^+) and (Zn^{2+}, Co^{2+}, In^{3+}, Cu^+) through the cation exchange. Figure 16 shows that the XRD patterns of the 3- and 4-cation systems are asymmetric or split peaks, indicating the phase separation, although the five-cation system shows a single-phase XRD pattern. This single phase was maintained even at 600°C. These results indicate that the obtained phase was a high-entropy phase.

5. Concluding Remarks

In this review, we have provided an overview of the synthesis methods, characterization, and properties of multi-element NPs, with a focus on high-entropy nanomaterials obtained by chemical syntheses. The number of studies on high-entropy nanomaterials increased sharply after the breakthrough in the synthesis reported in 2018. With the rapid development of this research topic, many kinds of synthesis methods have been reported from both top-down and bottom-up approaches; for example, pyrolysis, chemical synthesis, mechanochemical synthesis, and top-down methods. Among these methods, we focused on chemical synthesis based on solution chemistry because this is one of the best-developed methods to synthesize metal and oxide NPs.

The chemical synthesis methods for multi-element alloy NPs can be classified as hot-injection methods, continuous-flow reactor methods, heating-up methods, and others such as high-intensity ultrasound irradiation. Hot-injection methods and continuous-flow reactor methods are supposed to provide non-equilibrium solid-solution phases in addition to the equilibrium solid-solution phases because they allow concurrent reduction of the constituent ions and lead to kinetically stable phases. Moreover, the continuous-flow reactor methods enable chemical reactions at high pressures and temperatures by using a back-pressure valve, which further promotes the synthesis of novel multi-element alloy NPs. The synthesized nanoalloys are generally characterized through XRD and STEM-EDX to confirm their crystal structures and dispersion of the constituents. Very recently, the uniqueness of their electronic structures has also been uncovered by XPS and DFT calculations. Almost every atom in HEA NPs has different LDOS because of the different neighboring atomic configurations, even though the atoms are the same element. In other words, one atom in HEA loses its elemental identity and possesses new properties. Therefore, HEA NPs tend to have the “featureless” VB structure. The HEA NPs also show interesting properties such as very high activities for electrocatalytic reactions. Interestingly, the superior catalytic activity cannot be explained by the conventional *d*-band theory that is often used to predict and understand the properties of monometallic and binary alloy catalysts. This is probably because of the uniqueness in the electronic structure and atomic configuration of HEA NPs.

Multi-element ceramic NPs, including HEC NPs, have also been synthesized by chemical synthesis. Although the synthesis of HEO NPs often requires a calcination process at high temperature, some HEO NPs were prepared without calcination to avoid particle aggregation. Cation exchange is considered to be a powerful method to obtain not only sulfide, but also other multi-element ceramic NPs in a solution process. Multi-element ceramic NPs are also characterized by XRD and STEM-EDX. As well as alloys, they exhibit interesting properties such as high catalytic activity and ionic conductivity.

To date, the synthesis method for multi-element nanomaterials has not been widely studied compared with monometallic and binary systems. This is perhaps because a homogeneous solid-solution single phase consisting of multi-elements is likely to form at higher temperatures because of the larger configurational entropy. Generally, since the boiling points of solutions are relatively low, it is hard to perform a solution reaction at a very high temperature such as more than 1000°C, where the pyrolysis method is often performed to obtain multi-element nanomaterials. However, so far, solution-based chemical synthesis has allowed fine-tuning of the size, composition, morphology, nanostructure, etc., of monometallic and binary nanomaterials and greatly improved the properties of nanomaterials. Using non-chemical reduction methods, more than 20 elements were mixed into one NP,[111] multiple-elemental alloy NPs composed of more than 10 elements can be also obtained by a chemical reduction process. The ability of chemical

synthesis can be greatly extended by a further exploration of synthetic parameters such as reducing agents and solvents.

Although the solid-solution phase is drastically stabilized by a large configurational entropy of multi-elements, the formed solid-solution phases are not always the most thermodynamically stable. Some phases are not enthalpically favored and kinetically stabilized in chemical synthesis conditions. Since atomic diffusion in NPs does not significantly occur at RT, once those solid-solution phases are formed in chemical syntheses, they would be stable at RT regardless of being in an equilibrium phase or not. However, when the critical temperature of the alloy is above the temperature where the atomic diffusion in the particle significantly occurs, the solid-solution phase may undergo phase transitions such as phase separation at several hundred degrees. This point should be considered for future applications.

In addition to the synthesis, the development in the structural analysis, especially surface structure at the atomic scale, is also demanded to further elucidate their catalytic mechanism. Recently, a quantitative characterization of the alloying state in ternary alloy nanoparticles was succeeded by a combination of STEM-EDS analysis and a statistical approach.[112] However, in multi-element NPs, new technology including the higher detection sensitivity of instruments would be required because of the low-intensity signals from a fewer number of multi-elements in nano(angstrom)-scale space.

Furthermore, since multi-element nanomaterials provide a vast research space because of the almost infinite combinations of elements and compositions, new advanced technologies such as high-throughput screening coupled with data science, atomic-scale analysis, neural network potential,[113] and quantum computer for efficient exploration, would be required. We believe that solution-based chemical synthesis combined with these techniques can make significant contributions to the development of multi-element nanomaterials, and that a variety of new materials with exciting properties will be discovered by fully using the available elements hereafter.

Acknowledgements

The authors acknowledge the support of JST-PRESTO (No. JPMJPR20A3), JSPS KAKENHI Grant-in-Aid for Specially Promoted Research (20H05623), a Grant-in-Aid for Scientific Research (B) (No. 21H01762), and a Grant-in-Aid for Young Scientists (No. 22K14565). This work was partially supported by the Demonstration Project of Innovative Catalyst Technology for Decarbonization through Regional Resource Recycling, the Ministry of the Environment, Government of Japan.

Keywords: multi-element • high entropy • nanoalloys • nanoceramics • chemical synthesis

[1] Z. Dai, H. Chen, R. Ding, Q. Lu, C. Zhang, Z. Yang, S. van der Zwaag, *Materials Science and Engineering: R: Reports* **2021**, *143*, 100590.
[2] R. Ma, S. Zhang, T. Wen, P. Gu, L. Li, G. Zhao, F. Niu, Q. Huang, Z. Tang, X. Wang, *Catal Today* **2019**, *335*, 20–30.
[3] M. H. Tsai, J. W. Yeh, *Mater Res Lett* **2014**, *2*, 107–123.
[4] J. W. Yeh, S. K. Chen, S. J. Lin, J. Y. Gan, T. S. Chin, T. T. Shun, C. H. Tsau, S. Y. Chang, *Adv Eng Mater* **2004**, *6*, 299–303.
[5] R. Z. Zhang, M. J. Reece, *J Mater Chem A Mater* **2019**, *7*, 22148–22162.
[6] R. Kubo, *J Physical Soc Japan* **1962**, *17*, 975–986.
[7] K. Kusada, H. Kobayashi, T. Yamamoto, S. Matsumura, N. Sumi, K. Sato, K. Nagaoka, Y. Kubota, H. Kitagawa, *J Am Chem Soc* **2013**, *135*, 5493–5496.
[8] Y. Nishida, K. Sato, T. Yamamoto, D. Wu, K. Kusada, H. Kobayashi, S. Matsumura, H. Kitagawa, K. Nagaoka, *Chem Lett* **2017**, *46*, 1254–1257.
[9] V. Iablokov, S. K. Beaumont, S. Alayoglu, V. v Pushkarev, C. Specht, J. Gao, a P. Alivisatos, N. Kruse, G. a Somorjai, *Nano Lett* **2012**, *12*, 3091–3096.
[10] Y. Xia, Y. Xiong, B. Lim, S. E. Skrabalak, *Angewandte Chemie - International Edition* **2009**, *48*, 60–103.
[11] I. Lee, F. Delbecq, R. Morales, M. A. Albiter, F. Zaera, *Nat Mater* **2009**, *8*, 132–138.
[12] G. Chen, J. Zhang, A. Gupta, F. Rosei, D. Ma, *New Journal of Chemistry* **2014**, *38*, 1827–1833.
[13] Y. Shi, Z. Lyu, M. Zhao, R. Chen, Q. N. Nguyen, Y. Xia, *Chem Rev* **2021**, *121*, 649–735.
[14] Ö. Metin, X. Sun, S. Sun, *Nanoscale* **2013**, *5*, 910–912.
[15] F. Wang, K. Kusada, D. Wu, T. Yamamoto, T. Toriyama, S. Matsumura, Y. Nanba, M. Koyama, H. Kitagawa, *Angewandte Chemie - International Edition* **2018**, *0395*, 4505–4509.
[16] Z. Liu, E. T. Ada, M. Shamsuzzoha, G. B. Thompson, D. E. Nikles, *Chemistry of Materials* **2006**, *18*, 4946–4951.
[17] K. Kusada, H. Kitagawa, *Advanced Materials* **2016**, *28*, 1129–1142.
[18] Q. Zhang, K. Kusada, H. Kitagawa, *Chempluschem* **2021**, *86*, 504–519.
[19] Q. Zhang, K. Kusada, D. Wu, N. Ogiwara, T. Yamamoto, T. Toriyama, S. Matsumura, S. Kawaguchi, Y. Kubota, T. Honma, H. Kitagawa, *Chem Sci* **2019**, *10*, 5133–5137.
[20] J. Liu, J. Huang, W. Niu, C. Tan, H. Zhang, *Chem Rev* **2021**, *121*, 5830–5888.
[21] T. Wakisaka, K. Kusada, D. Wu, T. Yamamoto, T. Toriyama, S. Matsumura, H. Akiba, O. Yamamuro, K. Ikeda, T. Otomo, N. Palina, Y. Chen, L. S. R. Kumara, C. Song, O. Sakata, W. Xie, M. Koyama, Y. Kubota, S. Kawaguchi, R. L. Arevalo, S. M. Aspera, E. F. Arguelles, H. Nakanishi, H. Kitagawa, *J Am Chem Soc* **2020**, *142*, 1247–1253.
[22] Q. Zhang, K. Kusada, D. Wu, T. Yamamoto, T. Toriyama, S. Matsumura, S. Kawaguchi, Y. Kubota, H. Kitagawa, *J Am Chem Soc* **2022**, *144*, 4224–4232.
[23] K. Kusada, D. Wu, Y. Nanba, M. Koyama, T. Yamamoto, X. Q. Tran, T. Toriyama, S. Matsumura, A. Ito, K. Sato, K. Nagaoka, O. Seo, C. Song, Y. Chen, N. Palina, L. S. R. Kumara, S. Hiroi, O. Sakata, S. Kawaguchi, Y. Kubota, H. Kitagawa, *Advanced Materials* **2021**, *33*, 2005206.
[24] D. Wu, K. Kusada, Y. Nanba, M. Koyama, T. Yamamoto, T. Toriyama, S. Matsumura, O. Seo, I. Gueye, J. Kim, L. S. Rosantha Kumara, O. Sakata, S. Kawaguchi, Y. Kubota, H. Kitagawa, *J Am Chem Soc* **2022**, *144*, 3365–3369.
[25] B. Zhang, X. Zheng, O. Voznyy, R. Comin, M. Bajdich, M. García-Melchor, L. Han, J. Xu, M. Liu, L. Zheng, F. P. G. de Arquer, C. T. Dinh, F. Fan, M. Yuan, E. Yassitepe, N. Chen, T. Regier, P. Liu, Y. Li, P. de Luna, A. Janmohamed, H. L. Xin, H. Yang, A. Vojvodic, E. H. Sargent, *Science (1979)* **2016**, *352*, 333–337.
[26] L. Hu, P. Xie, R. Shahbazian-Yassar, Y. Yao, S. D. Lacey, J. Li, R. J. Jacob, C. Wang, H. Xie, A. Nie, Z. Huang, F. Chen, M. Rehwoldt, D. Yu, M. R. Zachariah, T. Pu, *Science (1979)* **2018**, *359*, 1489–1494.
[27] H.-J. Qiu, G. Fang, J. Gao, Y. Wen, J. Lv, H. Li, G. Xie, X. Liu, S. Sun, *ACS Mater Lett* **2019**, *1*, 526–533.
[28] C. Zhan, Y. Xu, L. Bu, H. Zhu, Y. Feng, T. Yang, Y. Zhang, Z. Yang, B. Huang, Q. Shao, X. Huang, *Nat Commun* **2021**, *12*, 6261.
[29] T. Yu, Y. Zhang, Y. Hu, K. Hu, X. Lin, G. Xie, X. Liu, K. M. Reddy, Y. Ito, H. J. Qiu, *ACS Mater Lett* **2022**, *4*, 181–189.
[30] H. Li, Y. Han, H. Zhao, W. Qi, D. Zhang, Y. Yu, W. Cai, S. Li, J. Lai, B. Huang, L. Wang, *Nat Commun* **2020**, *11*, 5437.
[31] N. L. N. Broge, M. Bondesgaard, F. Søndergaard-Pedersen, M. Roelsgaard, B. B. Iversen, *Angewandte Chemie - International Edition* **2020**, *59*, 21920–21924.
[32] Y. Li, Y. Liao, J. Zhang, E. Huang, L. Ji, Z. Zhang, R. Zhao, Z. Zhang, B. Yang, Y. Zhang, B. Xu, G. Qin, X. Zhang, *Angewandte Chemie - International Edition* **2021**, *60*, 27113–27118.
[33] K. Mori, N. Hashimoto, N. Kamiuchi, H. Yoshida, H. Kobayashi, H. Yamashita, *Nat Commun* **2021**, *12*, 3884.
[34] Q. Dong, M. Hong, J. Gao, T. Li, M. Cui, S. Li, H. Qiao, A. H. Brozena, Y. Yao, X. Wang, G. Chen, J. Luo, L. Hu, *Small* **2022**, *18*, 2104761.
[35] H. Chen, Y. Sun, S. Yang, H. Wang, W. Dmowski, T. Egami, S. Dai, *Chemical Communications* **2020**, *56*, 15056–15059.
[36] T. Wang, H. Chen, Z. Yang, J. Liang, S. Dai, *J Am Chem Soc* **2020**, *142*, 4550–4554.
[37] H. Xu, Z. Zhang, J. Liu, C.-L. Do-Thanh, H. Chen, S. Xu, Q. Lin, Y. Jiao, J. Wang, Y. Wang, Y. Chen, S. Dai, *Nat Commun* **2020**, *11*, 3908.

[38] D. Wang, Z. Liu, S. Du, Y. Zhang, H. Li, Z. Xiao, W. Chen, R. Chen, Y. Wang, Y. Zou, S. Wang, *J Mater Chem A Mater* **2019**, *7*, 24211–24216.
[39] R. Nandan, M. Y. Rekha, H. R. Devi, C. Srivastava, K. K. Nanda, *Chemical Communications* **2021**, *57*, 611–614.
[40] M. S. Lal, R. Sundara, *ACS Appl Mater Interfaces* **2019**, *11*, 30846–30857.
[41] M. Cui, C. Yang, B. Li, Q. Dong, M. Wu, S. Hwang, H. Xie, X. Wang, G. Wang, L. Hu, *Adv Energy Mater* **2021**, *11*, 2002887.
[42] Q. F. He, P. H. Tang, H. A. Chen, S. Lan, J. G. Wang, J. H. Luan, M. Du, Y. Liu, C. T. Liu, C. W. Pao, Y. Yang, *Acta Mater* **2021**, *216*, 117140.
[43] S. Gao, S. Hao, Z. Huang, Y. Yuan, S. Han, L. Lei, X. Zhang, R. Shahbazian-Yassar, J. Lu, *Nat Commun* **2020**, *11*, 2016.
[44] K. Huang, B. Zhang, J. Wu, T. Zhang, D. Peng, X. Cao, Z. Zhang, Z. Li, Y. Huang, *J Mater Chem A Mater* **2020**, *8*, 11938–11947.
[45] M. Y. Rekha, N. Mallik, C. Srivastava, *Sci Rep* **2018**, *8*, 8737.
[46] T. Löffler, H. Meyer, A. Savan, P. Wilde, A. Garzón Manjón, Y.-T. Chen, E. Ventosa, C. Scheu, A. Ludwig, W. Schuhmann, *Adv Energy Mater* **2018**, *8*, 1802269.
[47] S. Li, J. Wang, X. Lin, G. Xie, Y. Huang, X. Liu, H. Qiu, *Adv Funct Mater* **2021**, *31*, 2007129.
[48] M. W. Glasscott, A. D. Pendergast, S. Goines, A. R. Bishop, A. T. Hoang, C. Renault, J. E. Dick, *Nat Commun* **2019**, *10*, 2650.
[49] X. Liu, D. Wang, Y. Li, *Nano Today* **2012**, *7*, 448–466.
[50] H. Kobayashi, K. Kusada, H. Kitagawa, *Acc Chem Res* **2015**, *48*, 1551–1559.
[51] J. Gu, Y. W. Zhang, F. Tao, *Chem Soc Rev* **2012**, *41*, 8050–8065.
[52] M. P. Singh, C. Srivastava, *Mater Lett* **2015**, *160*, 419–422.
[53] M. Liu, Z. Zhang, F. Okejiri, S. Yang, S. Zhou, S. Dai, *Adv Mater Interfaces* **2019**, *6*, 1900015.
[54] D. Wu, K. Kusada, T. Yamamoto, T. Toriyama, S. Matsumura, S. Kawaguchi, Y. Kubota, H. Kitagawa, *J Am Chem Soc* **2020**, *142*, 13833–13838.
[55] T. X. Nguyen, J. Patra, J. K. Chang, J. M. Ting, *J Mater Chem A Mater* **2020**, *8*, 18963–18973.
[56] F. Okejiri, Z. Zhang, J. Liu, M. Liu, S. Yang, S. Dai, *ChemSusChem* **2020**, *13*, 111–115.
[57] D. Wu, K. Kusada, T. Yamamoto, T. Toriyama, S. Matsumura, I. Gueye, O. Seo, J. Kim, S. Hiroi, O. Sakata, S. Kawaguchi, Y. Kubota, H. Kitagawa, *Chem Sci* **2020**, *11*, 12731–12736.
[58] Y. Chen, X. Zhan, S. L. A. Bueno, I. H. Shafei, H. M. Ashberry, K. Chatterjee, L. Xu, Y. Tang, S. E. Skrabalak, *Nanoscale Horiz* **2021**, *6*, 231–237.
[59] C. R. McCormick, R. E. Schaak, *J Am Chem Soc* **2021**, *143*, 1017–1023.
[60] H. Qiao, M. T. Saray, X. Wang, S. Xu, G. Chen, Z. Huang, C. Chen, G. Zhong, Q. Dong, M. Hong, H. Xie, R. Shahbazian-Yassar, L. Hu, *ACS Nano* **2021**, *15*, 14928–14937.
[61] M. Kheradmandfard, H. Minouei, N. Tsvetkov, A. K. Vayghan, S. F. Kashani-Bozorg, G. Kim, S. I. Hong, D.-E. Kim, *Mater Chem Phys* **2021**, *262*, 124265.
[62] G. Feng, F. Ning, J. Song, H. Shang, K. Zhang, Z. Ding, P. Gao, W. Chu, D. Xia, *J Am Chem Soc* **2021**, *143*, 17117–17127.
[63] E. Shen, X. Song, Q. Chen, M. Zheng, J. Bian, H. Liu, *ChemElectroChem* **2021**, *8*, 260–269.
[64] D. Zhang, H. Zhao, X. Wu, Y. Deng, Z. Wang, Y. Han, H. Li, Y. Shi, X. Chen, S. Li, J. Lai, B. Huang, L. Wang, *Adv Funct Mater* **2021**, *31*, 2006939.
[65] D. Zhang, Y. Shi, H. Zhao, W. Qi, X. Chen, T. Zhan, S. Li, B. Yang, M. Sun, J. Lai, B. Huang, L. Wang, *J Mater Chem A Mater* **2021**, *9*, 889–893.
[66] N. Wang, P. Cao, S. Sun, H. Ma, H. Ma, *Inorg Chem* **2021**, *60*, 3471–3478.
[67] F. Okejiri, Z. Yang, H. Chen, C.-L. Do-Thanh, T. Wang, S. Yang, S. Dai, *Nano Res* **2022**, *15*, 4792–4798.
[68] Y. Maruta, K. Kusada, D. Wu, T. Yamamoto, T. Toriyama, S. Matsumura, O. Seo, S. Yasuno, S. Kawaguchi, O. Sakata, Y. Kubota, H. Kitagawa, *Chemical Communications* **2022**, *58*, 6421–6424.
[69] K. Kusada, T. Yamamoto, T. Toriyama, S. Matsumura, K. Sato, K. Nagaoka, K. Terada, Y. Ikeda, Y. Hirai, H. Kitagawa, *Journal of Physical Chemistry C* **2021**, *125*, 458–463.
[70] H. Minamihara, K. Kusada, D. Wu, T. Yamamoto, T. Toriyama, S. Matsumura, L. S. R. Kumara, K. Ohara, O. Sakata, S. Kawaguchi, Y. Kubota, H. Kitagawa, *J Am Chem Soc* **2022**, *144*, 11525–11529.
[71] A. Moghtada, R. Ashiri, *Ultrason Sonochem* **2018**, *41*, 127–133.
[72] A. Gedanken, *Ultrason Sonochem* **2004**, *11*, 47–55.
[73] K. Kusada, D. Wu, H. Kitagawa, *Chemistry - A European Journal* **2020**, *26*, 5105–5130.
[74] J. Monzó, M. T. M. Koper, P. Rodriguez, *ChemPhysChem* **2012**, *13*, 709–715.
[75] Y. Borodko, H. S. Lee, S. H. Joo, Y. Zhang, G. Somorjai, *Journal of Physical Chemistry C* **2010**, *114*, 1117–1126.
[76] K. M. Koczkur, S. Mourdikoudis, L. Polavarapu, S. E. Skrabalak, *Dalton Transactions* **2015**, *44*, 17883–17905.
[77] K. Kusada, H. Kitagawa, *Mater Horiz* **2022**, *9*, 547–558.
[78] A. Knauer, A. Thete, S. Li, H. Romanus, A. Csáki, W. Fritzsche, J. M. Köhler, *Chemical Engineering Journal* **2011**, *166*, 1164–1169.
[79] S. Cattaneo, S. Althahban, S. J. Freakley, M. Sankar, T. Davies, Q. He, N. Dimitratos, C. J. Kiely, G. J. Hutchings, *Nanoscale* **2019**, *11*, 8247–8259.
[80] Y. Hashiguchi, F. Watanabe, T. Honma, I. Nakamura, S. S. Poly, T. Kawaguchi, T. Tsuji, H. Murayama, M. Tokunaga, T. Fujitani, *Colloids Surf A Physicochem Eng Asp* **2021**, *620*, 126607.
[81] T. Gu, C. Zheng, F. He, Y. Zhang, S. A. Khan, T. A. Hatton, *Lab Chip* **2018**, *18*, 1330–1340.
[82] Y. Zhou, D. Wang, X. Kang, D. Zhang, X. Dou, X. Wang, G. Guo, *Nanoscale* **2020**, *12*, 12647–12654.
[83] K. S. Kim, S. Choi, J. H. Cha, S. H. Yeon, H. Lee, *J Mater Chem* **2006**, *16*, 1315–1317.
[84] P. Zhang, Y. Gong, Y. Lv, Y. Guo, Y. Wang, C. Wang, H. Li, *Chemical Communications* **2012**, *48*, 2334–2336.
[85] H. Lu, P. Zhang, Z. A. Qiao, J. Zhang, H. Zhu, J. Chen, Y. Chen, S. Dai, *Chemical Communications* **2015**, *51*, 5910–5913.
[86] J. K. Nørskov, F. Abild-Pedersen, F. Studt, T. Bligaard, *Proc Natl Acad Sci U S A* **2011**, *108*, 937–943.
[87] A. Vojvodic, J. K. Nørskov, F. Abild-Pedersen, *Top Catal* **2014**, *57*, 25–32.
[88] H. Xin, A. Vojvodic, J. Voss, J. K. Nørskov, F. Abild-Pedersen, *Phys Rev B* **2014**, *89*, 115114.
[89] C. M. Rost, E. Sachet, T. Borman, A. Moballegh, E. C. Dickey, D. Hou, J. L. Jones, S. Curtarolo, J.-P. Maria, *Nat Commun* **2015**, *6*, 8485.
[90] Z. Grzesik, G. Smoła, M. Stygar, J. Dąbrowa, M. Zajusz, K. Mroczka, M. Danielewski, *J Eur Ceram Soc* **2019**, *39*, 4292–4298.
[91] J. L. Braun, C. M. Rost, M. Lim, A. Giri, D. H. Olson, G. N. Kotsonis, G. Stan, D. W. Brenner, J. Maria, P. E. Hopkins, *Advanced Materials* **2018**, *30*, 1805004.
[92] Z. Rák, J. P. Maria, D. W. Brenner, *Mater Lett* **2018**, *217*, 300–303.
[93] J. Gild, M. Samiee, J. L. Braun, T. Harrington, H. Vega, P. E. Hopkins, K. Vecchio, J. Luo, *J Eur Ceram Soc* **2018**, *38*, 3578–3584.
[94] Y. Ma, Y. Ma, Q. Wang, S. Schweidler, M. Botros, T. Fu, H. Hahn, T. Brezesinski, B. Breitung, *Energy Environ Sci* **2021**, *14*, 2883–2905.
[95] G. M. Tomboc, X. Zhang, S. Choi, D. Kim, L. Y. S. Lee, K. Lee, *Adv Funct Mater* **2022**, 2205142.
[96] S. H. Albedwawi, A. AlJaberi, G. N. Haidemenopoulos, K. Polychronopoulou, *Mater Des* **2021**, *202*, 109534.
[97] A. Sarkar, R. Djenadic, N. J. Usharani, K. P. Sanghvi, V. S. K. Chakravadhanula, A. S. Gandhi, H. Hahn, S. S. Bhattacharya, *J Eur Ceram Soc* **2017**, *37*, 747–754.
[98] J. Dąbrowa, M. Stygar, A. Mikuła, A. Knapik, K. Mroczka, W. Tejchman, M. Danielewski, M. Martin, *Mater Lett* **2018**, *216*, 32–36.
[99] Y. Li, Y. Xu, W. Yang, W. Shen, H. Xue, H. Pang, *Small* **2018**, *14*, 1704435.
[100] C.-Y. Huang, C.-W. Huang, M.-C. Wu, J. Patra, T. Xuyen Nguyen, M.-T. Chang, O. Clemens, J.-M. Ting, J. Li, J.-K. Chang, W.-W. Wu, *Chemical Engineering Journal* **2021**, *420*, 129838.
[101] D. Bérardan, S. Franger, A. K. Meena, N. Dragoe, *J Mater Chem A Mater* **2016**, *4*, 9536–9541.
[102] M. H. Hsieh, M. H. Tsai, W. J. Shen, J. W. Yeh, *Surf Coat Technol* **2013**, *221*, 118–123.
[103] E. Castle, T. Csanádi, S. Grasso, J. Dusza, M. Reece, *Sci Rep* **2018**, *8*, 8609.
[104] J. Gild, Y. Zhang, T. Harrington, S. Jiang, T. Hu, M. C. Quinn, W. M. Mellor, N. Zhou, K. Vecchio, J. Luo, *Sci Rep* **2016**, *6*, 37946.
[105] R. Z. Zhang, F. Gucci, H. Zhu, K. Chen, M. J. Reece, *Inorg Chem* **2018**, *57*, 13027–13033.
[106] Z. Deng, A. Olvera, J. Casamento, J. S. Lopez, L. Williams, R. Lu, G. Shi, P. F. P. Poudeu, E. Kioupakis, *Chemistry of Materials* **2020**, *32*, 6070–6077.
[107] L. de Trizio, L. Manna, *Chem Rev* **2016**, *116*, 10852–10887.
[108] B. C. Steimle, J. L. Fenton, R. E. Schaak, *Science (1979)* **2020**, *367*, 418–424.
[109] J. L. Fenton, B. C. Steimle, R. E. Schaak, *Inorg Chem* **2019**, *58*, 672–678.
[110] A. E. Powell, J. M. Hodges, R. E. Schaak, *J Am Chem Soc* **2016**, *138*, 471–474.
[111] Y. Liao, Y. Li, R. Zhao, J. Zhang, L. Zhao, L. Ji, Z. Zhang, X. Liu, G. Qin, X. Zhang, *Natl Sci Rev* **2022**, *9*, DOI 10.1093/nsr/nwac041.
[112] X. Q. Tran, K. Aso, T. Yamamoto, W. Yang, Y. Kono, K. Kusada, D. Wu, H. Kitagawa, S. Matsumura, *ACS Nano* **2022**, *16*, 1612–1624.
[113] S. Takamoto, C. Shinagawa, D. Motoki, K. Nakago, W. Li, I. Kurata, T. Watanabe, Y. Yayama, H. Iriguchi, Y. Asano, T. Onodera, T. Ishii, T. Kudo, H. Ono, R. Sawada, R. Ishitani, M. Ong, T. Yamaguchi, T. Kataoka, A. Hayashi, N. Charoenphakdee, T. Ibuka, *Nat Commun* **2022**, *13*, 2991.

Entry for the Table of Contents

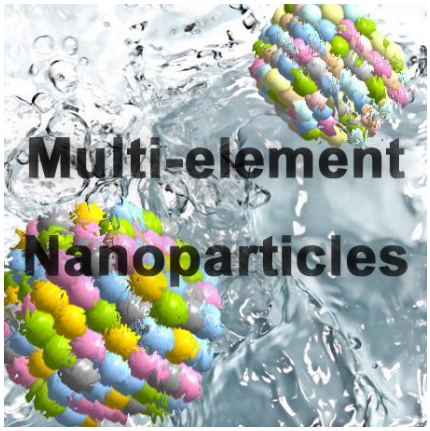

Multi-element nanoparticles (NPs) consisting of five or more elements often exhibit superior properties, including catalysis, compared with conventional NPs. Therefore, a variety of synthesis methods have recently been studied. In this review, we focus on chemical synthesis based on solution reactions for multi-element NPs and discuss their synthesis techniques, characterization, and properties.

Institute and/or researcher Twitter usernames: @ssc_kuchem